November 2017

Direct Digital Manufacturing of Multi-layer Wideband Ku-band Patch Antennas

Merve Kacar
University of South Florida, mervekacar@mail.usf.edu

Direct Digital Manufacturing of Multi-layer Wideband Ku-band Patch Antennas

by

Merve Kacar

A thesis submitted in partial fulfillment
of the requirements for the degree of
Master of Science in Electrical Engineering
Department of Electrical Engineering
College of Engineering
University of South Florida

Major Professor: Gokhan Mumcu, Ph.D.
Thomas Weller, Ph.D.
Jing Wang, Ph.D.

Date of Approval:
October 24, 2017

Keywords: 3-D printing, additive manufacturing, aperture coupled, microstrip antennas

DEDICATION

To my parents, and

to my beloved.

ACKNOWLEDGMENTS

First, I would like to thank my advisor Dr. Gökhan Mumcu for his guidance, support and patience throughout my study. I also wish to thank Dr. Thomas Weller, and Dr. Jing Wang for serving in my committee and for offering valuable suggestions. I hope to be able to benefit from their profound knowledge and experience in the future, as well.

I would also like to thank everyone at Sciperio Inc. including Casey Perkowski, Dr. Paul Deffenbaugh, and Dr. Kenneth Church. Especially, without Casey Perkowski's continuous support and dedication, fabrication of the components would not have been possible.

It has been a privilege to have the opportunity to do research as a member of the Wireless and Microwave Information Systems (WAMI) Center at USF. I would like to offer my special thanks to my former colleague Joshua Stephenson for his help during this work. For their help at USF, I would like to thank Denise Lugo, Arya Menon, Enrique Gonzalez, Ramiro Ramirez, Abdullah Qaroot, Dr. Eduardo Rojas for their support as friends and productive discussions as colleagues. Also, I would like to thank my friends Murat Karabacak, Ismail Uluturk, Orhun Aras Uzun, Merve Dogan, Burak Sarsilmaz, Emre Seyyal for their emotional support and patience.

Last, but by no means least, I would like to express my deepest gratitude to my parents Gül Kaçar and Erdinç Kaçar for their unconditional support throughout these years. Especially, it is not possible to thank my darling, Berker Peköz, enough for his love and support. I am very grateful for having such a wonderful family.

TABLE OF CONTENTS

LIST OF TABLES

LIST OF FIGURES

ABSTRACT

Design and performance of fully-printed Ku-band aperture coupled patch antennas fabricated by a direct digital manufacturing (DDM) approach that integrates fused deposition modeling (FDM) of acrylonitrile butadiene styrene (ABS) thermoplastic with in-situ micro-dispensing of conductive silver paste (CB028) are reported. Microstrip line characterizations are performed and demonstrate that misalignment of ABS substrate deposition direction with microstrip line micro-dispensing direction can degrade the effective conductivity up to 60% within the Ku-band, and must be taken into consideration in antenna array feed network designs. Specifically, over 125 µm thick ABS substrate, RF loss of 0.052 dB/mm is obtained at 18 GHz, demonstrating the feasibility of additively manufactured RF devices within the Ku-band. By varying ABS infill ratios and resorting to multi-layer printing with custom substrate thicknesses, single and stacked patch antennas are designed, fabricated, and characterized with bandwidth performances up to 35%, and radiation efficiencies up to 90%. This extensive utilization of the design flexibilities provided by the direct digital manufacturing (i.e. customized substrate thicknesses, multiple substrates with varying infill ratios, and in-situ micro-dispensing of conductors) distinguishes the present work from the recently reported 3-D printed antennas. Compared to the existing work in literature, the antennas presented within this thesis stand out as being fully printed structures, operating in higher frequency range (i.e. Ku-band), and exhibiting high radiation efficiencies with wide bandwidth performances.

CHAPTER 1:

INTRODUCTION

Additive manufacturing (AM) or 3-D printing is the process of building an object layer-by-layer using a 3-D model data. Direct digital manufacturing (DDM) refers to the digitally defined fabrication process which does not necessitate significant human interaction or special tooling. From bioprinting organs [2] to electronics [3], AM became an extensive research area [4, 5]. DDM has started as a rapid prototyping method for testing a new product; however, it developed into a whole fabrication process for end-use products [6]. It is a low-cost technology, especially for custom-made products. Other than being a cost-effective method, it introduces new design solutions for engineers. Particularly in RF/microwave applications, DDM not only provides cost-effective, compact solutions with a one-pass process but offers enhanced design flexibilities in terms of material choices, layer thicknesses, and substrate shapes to enhance the RF device performances [7].

Recent literature has investigated passive RF and microwave components that are fabricated using various DDM technologies. For example, reference [8] has presented the characterization of substrates fabricated using stereolithography (SLA), finite deposition modeling (FDM) and micro-dispensed nanoparticle silver inks up to 10 GHz using transmission line characterizations. Reference [9] has demonstrated characterization of low-loss aerosol jet printed (AJP) transmission lines and vertical interconnects up to 40 GHz. Reference [10] has presented K-band coplanar waveguides fabricated with a hybrid approach of additive manufacturing and laser machining to improve the effective conductivity. Metal-pipe rectangular waveguides fabricated by FDM for X-band and SLA for W-band applications

are provided and compared in [11]. Reference [12] has presented examples of passive RF components such as flexible inkjet-printed capacitor, inductor, AMC-backed monopole antenna and SIW. Reference [13] has demonstrated a multi-layer fully-printed RF front end fabricated by in-situ FDM of acrylonitrile butadiene styrene (ABS) and micro-dispensing of silver ink. Reference [14] has presented ink-jet printed patch antennas on origami-folded cube fabricated by polymer polyjetting. Reference [15] has also demonstrated 3-D printed folded frequency selective structures.

Previously, DDM antennas with high radiation efficiencies have been demonstrated. However, these demonstrations have been limited to frequencies that are below 10 GHz. For example, reference [13]'s multi-layer RF front end demonstration is at 2.45 GHz for a phased array unit cell. By utilizing a similar DDM approach, reference [16] presents a half-wave dipole antenna that is volumetrically embedded into the dielectric structure operating at 6 GHz. Reference [17] demonstrates a multi-material low-profile antenna with integrated AMC ground plane fabricated using FDM and additive manufacturing techniques such as micro-dispensing at 2.6 GHz. Reference [18] has also demonstrated the effect of infill percentage change on permittivity and loss tangent of a thermoplastic and rubber material around 2.4 GHz, paving the way for customized antenna substrates. On the other hand, existing antenna demonstrations above 10 GHz are mostly not-fully printed, by utilizing metallization as an external fabrication step over the additively manufactured dielectric parts. For instance, reference [19] demonstrates inkjet printed antennas operating at 24.5 GHz on flexible LCP laminates. Reference [20] utilizes stereolithography of polymers and metal plating to demonstrate low-cost Ku and Ka-band horn, reflector, and cavity antennas.

1.1 Aperture-coupled Patch Antennas

Since 1985 [21], aperture coupling as a feeding technique for microstrip patch antennas is widely used. Microstrip feed line and patch antenna are on different substrates while

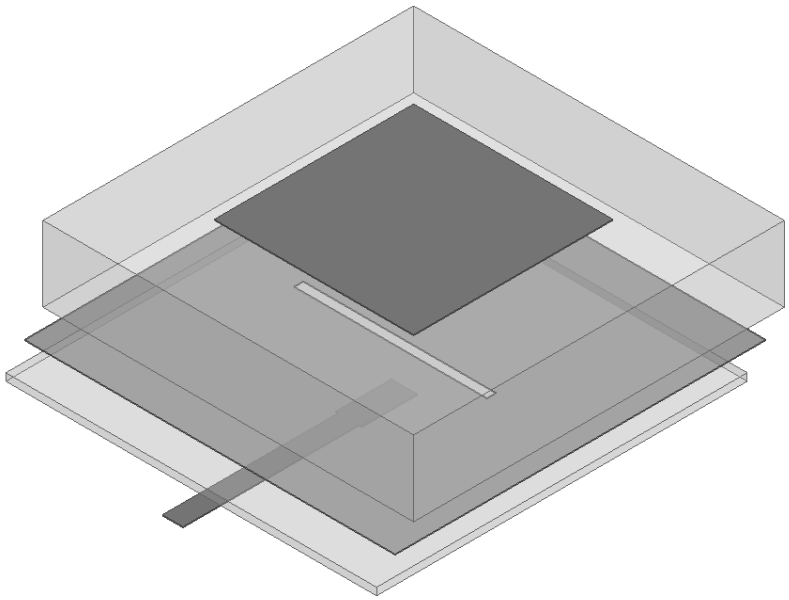

Figure 1.1: An aperture-coupled patch antenna

sharing a common ground. Figure 1.1 shows an expanded view of an aperture-coupled patch antenna. Microstrip line couples to the antenna through a slot on the ground plane. Since antenna and feed line substrates can be different in terms of both dielectric constant and thickness, impedance bandwidth can be increased by utilizing lower dielectric and higher thickness antenna substrate. High dielectric and high thickness cause increased spurious radiation and surface wave excitation. For phased array antenna applications, increased surface wave power causes mutual-coupling between the array elements, and a phenomenon caused scan blindness [22]. Additional space on the feed line substrate to accommodate T/R module components such as phase shifters, amplifiers, bias network is another advantage of this feeding technique for phased array applications.

Aperture-coupled patch antennas are analyzed in [23, 24] using Green's functions. References [25, 26] provide a detailed explanation of microstrip patch antennas and aperture coupling. In addition to single polarized aperture-coupled patch antennas, dual and circularly polarized antennas are also presented in [27] using orthogonal slots. Reference [28]

presents dual-linear polarized aperture-coupled circular patch antennas with C-shaped slot for better isolation and wider axial ratio bandwidth. Stacked patch antennas [29] are widely utilized where another patch is placed above the lower patch to improve the bandwidth. In [30], stacked patch and H-shaped slots are used to improve bandwidth and reduce cross-polarization levels.

Aperture-coupled patch antennas have design flexibilities such as substrate thicknesses and dielectric constant. However, these flexibilities can only be utilized in discrete steps in conventional fabrication methods. For example, substrate thicknesses are available in certain thicknesses, and permittivity variation can only be achieved by either a different material usage or micro-fabrication. DDM enables levels of flexibility that are not available in other methods. While multi-layer antennas are fabricated in many process steps (photolithography, etching, bonding) with conventional methods, DDM offers a one-pass process.

1.2 Direct Digital Manufacturing Techniques

According to ASTM [31], additive manufacturing processes can be divided into six categories which are fused deposition modeling, stereolithography, direct metal laser sintering (DMLS), selective laser sintering (SLS), binder jetting and polyjet. Polymers, ceramics, hybrids and metals can be used depending on the process category [32]. Stereolithography refers to a process where a part is built by UV cured liquid photopolymer layers. References [33–35] have demonstrated high-frequency antennas fabricated using polymer and ceramic SLA. SLS is laser sintering of powdered material into a solid form where the materials can be polymers, ceramics - mostly nylon. DMLS is quite similar to SLS; however, it is for metal powder. Also, instead of locally heating and melting the powder, DMLS can fully melt into a homogeneous part in addition to sintering. Binder jetting or ink-jet printing also uses powder material; however, a liquid binding adhesive is selectively deposited on the places. Metals, ceramics, and polymers can be printed using binder-jetting. References [36–

38] have presented metallic binder-jetting and SLS for high-frequency antennas. Polyjet is quite similar to binder jetting. Instead of liquid binding adhesive, polyjet technique dispenses liquid photopolymer to the bed and cures with UV light. Due to their multi-layer printing capabilities, fused deposition modeling for printing substrate materials and micro-dispensing for metallization are utilized in this work. These techniques will be detailed in the following sections.

1.2.1 Fused Deposition Modeling

Fused deposition modeling refers to a process where the part is built layer-by-layer using a heated and softened polymer filament extruded from a nozzle. Some of the commonly used materials in FDM process are ABS, polylactic acid (PLA), ULTEM, polycarbonate (PC), PC-ABS, polyether ether ketone (PEEK). Thermoplastic materials are advantageous due to their heat resistance properties. Thermoplastic material is chosen depending on the requirement of the application such as glass transition temperature, strength, RF performance and chemical resistance. Hybrid materials such as ceramic composites have been developed in order to achieve certain RF characteristics [39]. Figure 1.2 shows how the material is extruded from the nozzle during a FDM process. The nozzle is heated up to high temperatures (200°C-240°C) to melt the filament. Since the printed material cools down rapidly, the bottom of the part can warp due to high contraction and stress. Cooling can be slowed down using a heated printer bed where the temperature is generally adjusted to 80°C - 130°C. High-frequency applications require a smooth surface profile, specifically for surfaces to be metallized. Surface characteristic of FDM is explained in detail and characterized in Chapter 2. After the part is designed, STL file is imported to a slicer software. Slicer software converts the 3-D model to a path file for the printer. After inputting information about filament and print settings such as filament diameter, layer thickness, infill density, speed, and extrusion multiplier, G-code is generated. G-code controls the movement of the printer

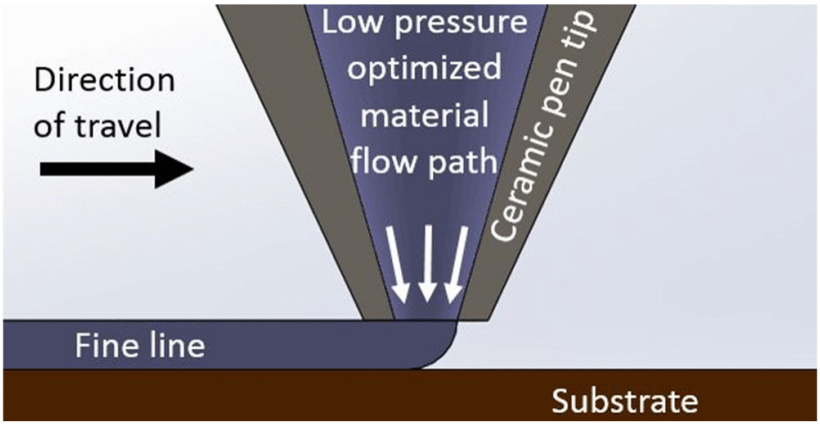

Figure 1.2: Material extrusion process [1] © 2017, IEEE

nozzle or bed, speed and amount of material extrusion. While G-code can be converted into other formats such as PGM files, it is commonly used in FDM printers. Finally, G-code is imported to the printer software to build the part.

1.2.2 Micro-dispensing

Micro-dispensing means that the fluid material is deposited in less than microlitre of volume. A smaller amount of volume (less than 100 picoliters in this work) can be achieved with high precision pumps. Materials such as dielectric and conductive inks, epoxies can be printed using this technique. Compared to binder-jet and polyjet printers, it can deposit liquids with a wider range of viscosities. Due to smaller nozzle sizes, jet printers can print smaller features down to 5 µm. Additional sintering process increases the conductivity of the metallic inks. Pressure and valve opening are the main parameters affecting the amount of material coming out of the nozzle. In addition to these parameters, speed also determines the single pass line width and thickness. Another parameter is the tip-to-surface distance which affects the line width consistency.

1.3 Scope of the Thesis

The scope of this thesis is to advance the applicability of DDM antennas into the Ku-band through microstrip line based conductivity characterizations and a multi-layer wide-band dual-polarized antenna realization that harnesses the available design flexibilities. The following chapters include performance results of the proposed antennas.

1.4 Contributions

Fully-printed wideband Ku-band aperture coupled stacked patch antennas fabricated by FDM of ABS filaments and in-situ micro-dispensing of silver paste CB028 are presented. The conductivity of micro-dispensed CB028 lines is investigated for the first time within the Ku-band and demonstrated to vary by 60% with respect to the line vs ABS filament deposition direction. Conductive losses associated with surface roughness of FDM of ABS filaments are minimized by resorting to 25 µm thick filament deposition thickness. Specifically, 0.052 dB/mm loss at 18 GHz is achieved over 125 µm thick ABS substrates. This characterization will pave the way for future feed network development that will integrate active devices (e.g. switches and amplifiers). By varying infill ratios and thicknesses of the antenna substrates, a dual-polarized stacked patch antenna with 35% bandwidth and 80% radiation efficiency is achieved. The fully-printed structure, operating within higher microwave frequencies (Ku-band), high radiation efficiency, and utilizing design flexibilities provided by DDM distinguish this work from the recently reported AM antennas.

1.5 Thesis Outline

The work is organized as follows. In Chapter II, microstrip lines fabricated by FDM of ABS and micro-dispensing of silver ink are characterized to extract the effective conductivity at higher microwave frequencies. TRL calibration standards are utilized to improve the

accuracy of the measurement. Effect of FDM direction vs. microstrip direction is investigated at Ku-band.

Chapter III presents the design, tolerance analysis and performance of a fully-printed single layer aperture coupled patch antenna. By employing a multi-layer printing approach, wideband and high efficiency performance are achieved using design flexibilities of DDM such as dielectric constant and custom substrate thicknesses. Power-handling properties of the antenna are also investigated. Thermal images of the antennas are taken at different input power levels and compared to thermal simulation results obtained by Ansys HFSS and Workbench simulations.

Chapter IV extends this design to a fully-printed wideband dual-linear polarized aperture coupled stacked patch antenna integrated with a switch. The antenna design is suitable for 1-D array applications, which has also been demonstrated.

Chapter V summarizes the contributions and concludes the thesis.

CHAPTER 2:

RF CHARACTERIZATION OF DIRECT DIGITAL MANUFACTURED TRANSMISSION LINES

In this chapter, effective conductivity at higher microwave frequencies is investigated through microstrip line characterizations. Microstrip lines are fabricated by FDM of ABS and micro-dispensing of silver ink. Effect of FDM direction vs. microstrip direction is investigated in order to maximize the efficiency of the feed network. TRL calibration standards are utilized to improve the accuracy of the measurement.

2.1 Fabrication

nScrypt 3Dn-Tabletop printer in Figure 2.1 is used for the devices presented in this thesis[1]. For substrate material, acrylonitrile butadiene styrene (ABS) which is a common amorphous thermoplastic polymer is used. ABS is printed in 25 µm layers; since it provides a smoother surface profile which is explained in detail in the following section. Feasible minimum layer thickness is 15 µm; while thick layers (> 150µm) can be printed with a bigger dispensing tip size. For both FDM and micro-dispensing, ceramic 75 µm I.D. / 125 µm O.D. tip provides adequate minimum line width of 125 µm. Minimum line width is proportional to the tip size. Small line widths can not be achieved with big tip sizes, since control over the volume of the extruded material becomes harder. Extrusion nozzle temperature for ABS and

[1]The content of this chapter is published in [40]. © 2017 IEEE. Reprinted, with permission, from M. Kacar, C. Perkowski, P. Deffenbaugh, J. Booth, G. Mumcu, and T. Weller, "Wide- band ku-band antennas using multi-layer direct digital manufacturing," in Proceedings of 2017 IEEE AP-S Symposium on Antennas and Propagation and USNC-URSI Radio Science Meeting, July 2017, pp. 1–2.

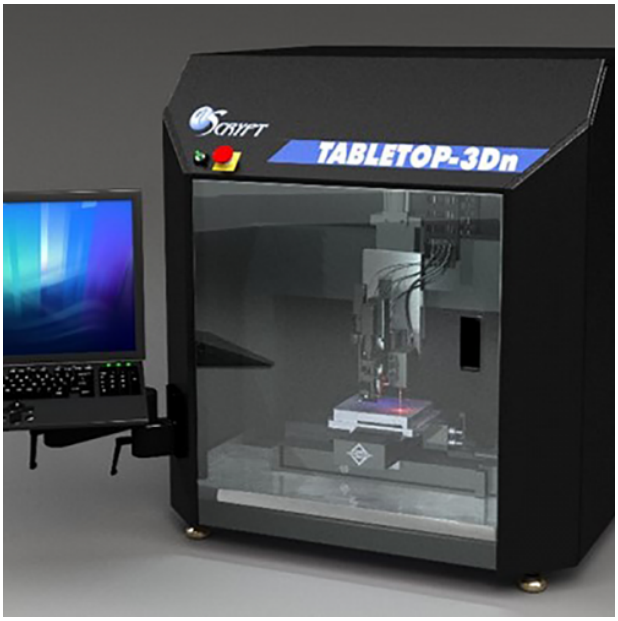

Figure 2.1: nScrypt Tabletop-3Dn printer

Table 2.1: FDM parameters

Parameter	Value
Printing speed	20 mm/s
Nozzle temperature	240°C
Bed temperature	90°C
Layer height	25 um
Line width	125 um

bed temperature are adjusted to 240°C and 90°C, respectively. Since ABS is an amorphous material, it doesn't have a melting temperature. However, common practice is 230°C - 240°C nozzle temperature. High printing temperature improves the adhesion between the layers, and printer bed temperature decreases the chance of warping on the base of the part. In addition to heating the printer bed, a mixture of ABS and acetone is applied to the printer bed surface to improve the adhesion and prevent warping. Table 2.1 shows the FDM parameters used in this work.

For metallization, DuPont CB028 silver conductor with a viscosity of 15-30 Pa·S is utilized. Prior to printing, conductive ink is mixed in a spinner to get a homogeneous

mixture. Micro-dispensing refers to a system which can deposit liquid materials with high control over the volume (i.e. 100 picoliters in this paper). A high precision and speed pump system from nScrypt is utilized. A path file is generated from DXF files using the PCAD software. Generated path file is imported to the printer software to use the pump. However, single pass line width needs to be adjusted prior to micro-dispensing. One of the main challenges of high-frequency device fabrication is the requirement for more precise control over the dimensions of conductive traces. Printing speed, pressure, and valve opening are the main parameters that affect the amount of material flow with respect to time. Table 2.2 shows the micro-dispensing parameters used in this thesis. Since CB028 has a relatively low viscosity, 5 psi pressure provides adequate material flow from the nozzle. Printing speed and valve opening are set to 20 mm/s and 0.12 mm, respectively. With lower pressure and high printing speeds, smaller line widths can be achieved. This parameter setting combination provides a single pass line width of 125 µm. The correct line width for the corresponding parameter setting combination should be imported to the PCAD software to achieve correct dimensions. Valve opening speed, waiting time after opening the valve and valve closing speed also affect the quality of micro-dispensing. High valve opening speeds may cause sputtering, and blotching in the beginning of the line. If the valve opening speed is too low or waiting time is not enough to let the material flow before starting to print, beginning of the line will be incomplete. Valve closing speed affects the end-of-line blotching. High valve closing speeds may reduce the extra amount of material at the end of the line; however, it may cause air sucked into the tip. The thickness of the metallic traces yields as 17 µm which is 6.7 times the skin depth at 18 GHz. A single pass of silver ink is printed since the thickness is sufficient for the frequency of operation. Once the micro-dispensing process is completed, CB028 is cured in-situ for 20 min to completely evaporate the solvent. While recommended temperature for curing CB028 is 160°C, glass transition temperature of ABS is 105°C. Beyond its glass transition temperature, ABS turns into a liquid with high viscosity.

Table 2.2: Micro-dispensing parameters

Parameter	Value
Printing speed	20 mm/s
Valve opening	120 um
Pressure	5 psi
Tip-to-surface distance	30 um

Therefore, bed temperature is used for curing which also provides in-situ curing; since there is not a significant difference in the conductivity between two cases [41].

Adhesion is also a significant issue for multi-material structures. To improve adhesion between the conductive ink and thermoplastic, a mixture of ABS and acetone is applied to the surface of cured ink prior to dispensing of ABS. Finally, multi-layer structures require highly accurate alignment. Prior to printing, DXF file for conductive ink should be carefully centered on the center of the substrate layers.

2.2 Microstrip Line Characterization

For high-frequency applications, the effect of surface and edge roughness on the effective conductivity becomes more pronounced. Transmission line characterization is utilized as a method to determine the effective conductivity.

Depending on the amount of extruded material, FDM commonly results in waviness on the surface. Increased surface roughness and ink leakage into the substrate can significantly degrade the effective conductivity. Surface ripple height can be minimized by increasing the extrusion multiplier; however, extruding extra material (over-extrusion) causes bumps on the surface which might lead to discontinuities on the deposited ink and open-circuits. Figure 2.2 shows the surface properties of FDM substrates as a result of under-extrusion and over-extrusion. Therefore, extrusion multiplier should be fine-tuned to achieve smooth surfaces while avoiding over-extrusion. Ripple height depends on the layer thickness. As layer thickness decreases, maximum possible ripple height decreases, and tun-

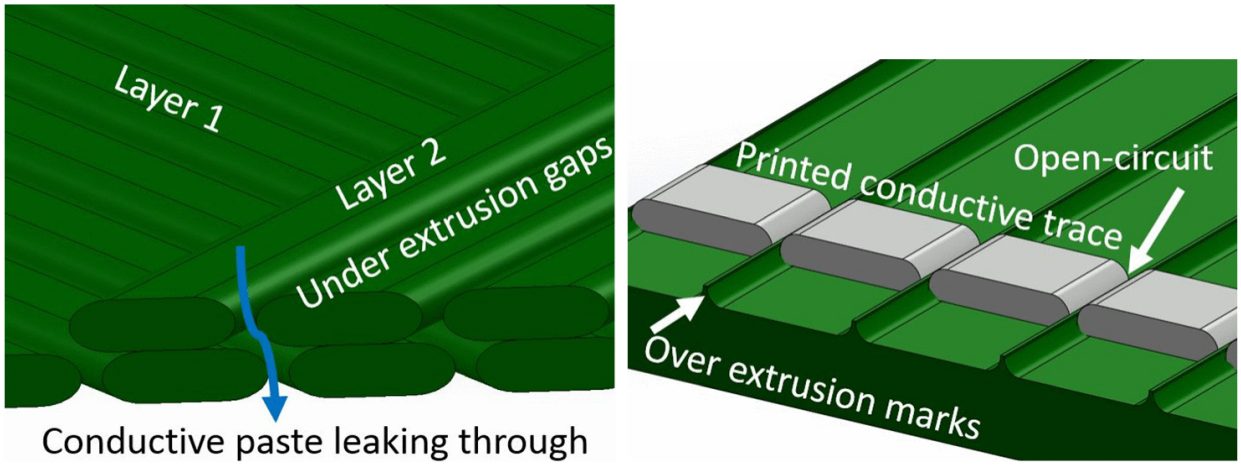

((a)) ((b))

Figure 2.2: (a) Under and (b) over extrusion surfaces [1] © 2017, IEEE

ing the extrusion multiplier becomes simpler. Minimum consistent thickness for ABS layers is 15 µm, which can be achieved with a small tip size. In this work, 25 µm layer thickness is used which provides low ripple height and feasible printing time. Selected tip size provides the 25 µm layer thickness and minimum line width for the micro-dispensing.

FDM direction vs. microstrip line direction affects the cross-section and edge roughness of the trace. As frequency increases, current becomes more concentrated on the edges of the strip. Therefore, the effect of edge roughness should be investigated at higher frequencies. Previous work [42] has demonstrated that the direction of the FDM varies the conductor loss at lower microwave frequencies (up to 5 GHz). Reference [16] has also investigated the effect of surface ripple at C-band by full-wave simulations. Microstrip lines are printed on 125 µm ABS substrate to characterize the effective conductivity for 0° (parallel to the trace), 45° and 90° (perpendicular) FDM orientations up to 20 GHz. Figure 2.3 shows the microscope images for 0° and 90° FDM orientations. It is seen on Figure 2.3 that 90° orientation case has more edge roughness than 0° orientation case.

The surface profile is measured with Dektak D-150. Ripple height and width are measured as 3 µm and 125 µm, respectively. Strip has 17 µm thickness at the center. Skin depth at 15 GHz is calculated as 3 µm, and conductor thickness is 5.7 times the skin depth.

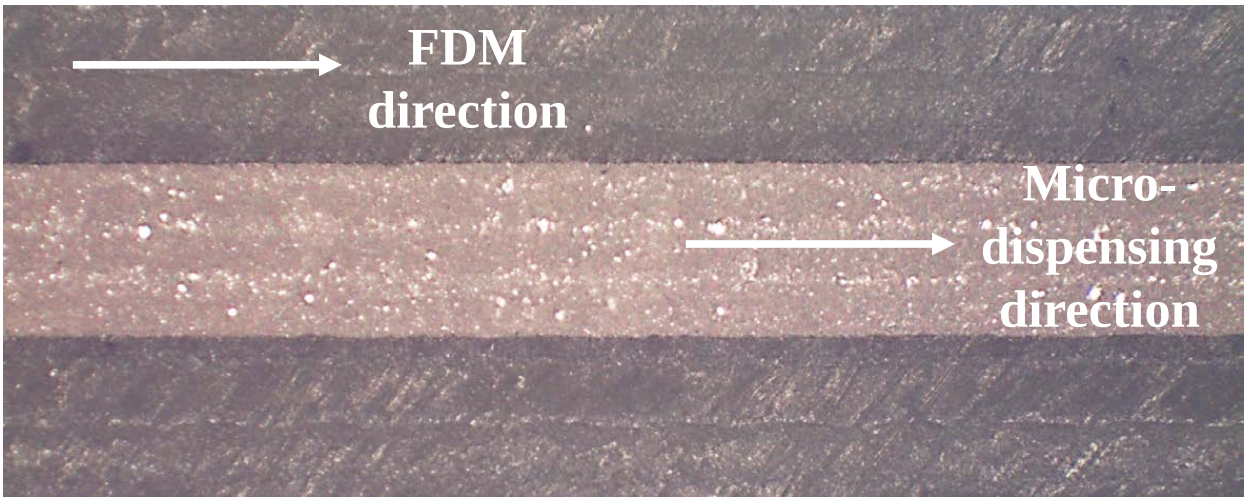

((a))

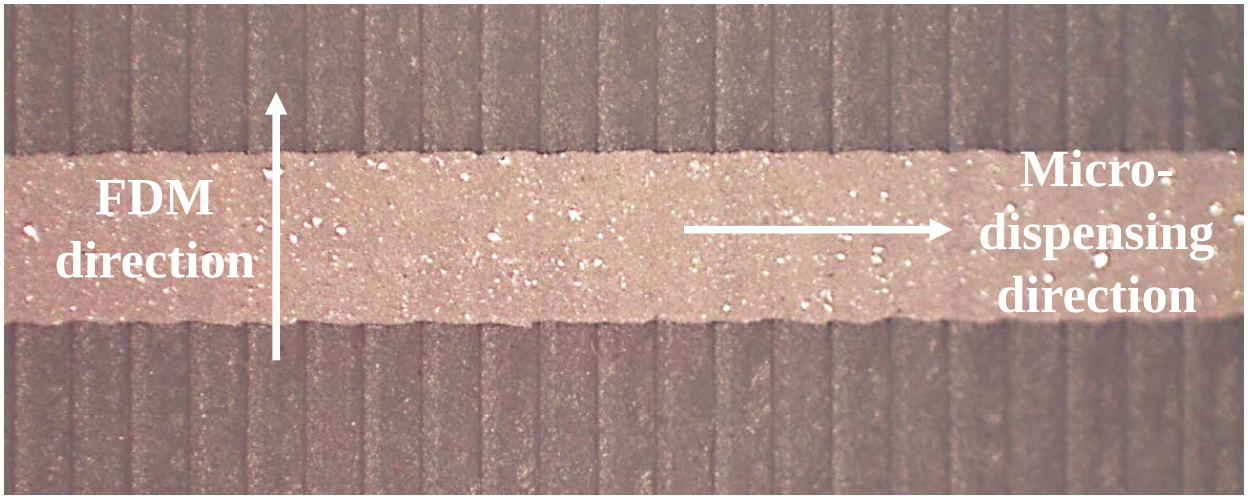

((b))

Figure 2.3: Microscope image of microstrip line for (a) 0° and (b) 90° FDM

Also, reference [10] has demonstrated the strip has a trapezoidal cross-section rather than a rectangular cross-section. Effect of strip cross-section on the attenuation is investigated with full-wave simulations. Figure 2.4 shows current density distribution on a strip with trapezoidal cross-section at 18 GHz, and insertion loss compared to a rectangular strip. It can be observed that the current is concentrated on the edges of the microstrip line. Effect of the cross-section increases with the frequency, and there is a significant increase in the attenuation. Reference [10] has also presented that laser machining edges of the metallic

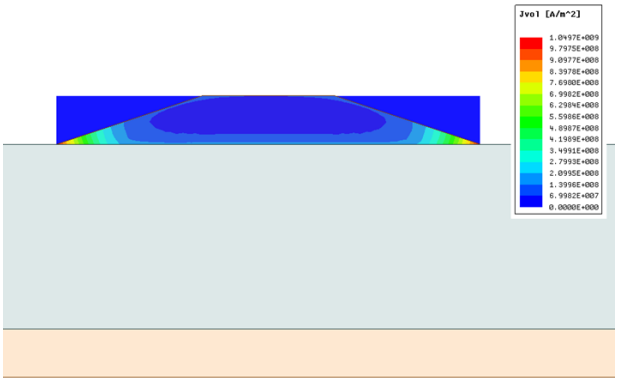

Figure 2.4: Current density distribution on trapezoidal strip

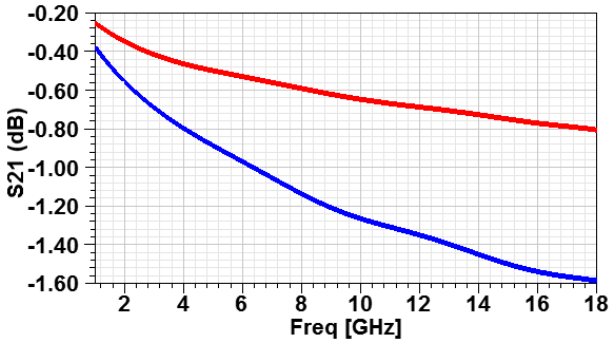

Figure 2.5: S_{21}(dB) for rectangular (red) and trapezoidal (blue) cross section

traces provides sharp edges and high conductivity region on the edges where current density is concentrated. Microstrip line with rectangular cross-section is simulated and effective conductivity is extracted for each orientation. Figure 2.6 shows the High Frequency Structure Simulator (HFSS) model of the microstrip line. Microstrip line is simulated using modal solution type with network analysis. Solution frequency is selected as the highest frequency which is 18 GHz. Maximum Delta-S is selected as 0.02. First order basis functions are used, and iterative solver is selected with 0.0001 relative residual. Microstrip line is simulated from 5 GHz to 18 GHz with interpolating sweep. Wave port is used for excitation. The width of the port is selected as 5 times the strip width, and height of the port is adjusted as 6 times the substrate thickness.

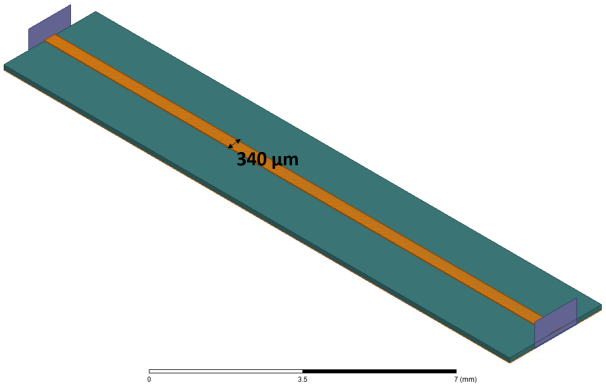

Figure 2.6: HFSS model of the microstrip line

Table 2.3: TRL standard lengths and frequency range of the delay lines

TRL Standards	Length (mm)	Frequency (GHz)
Through	3.5	-
Open	1.75	-
Delay Line 1	10.59	5-10.05
Delay Line 2	7.92	10-14.15
Delay Line 3	6.63	14.145-20

In [13], bulk DC conductivity of CB028 has characterized for various curing temperature using four-point probe and Van der Pauw techniques. The conductivity of CB028 for 90°C curing temperature is given as $2.62 \times 10^6 S/m$. Keysight N5227A network analyzer and Cascade Microtech probe station are used for S-parameter measurements. 650 µm pitch GSG probes from GGB Industries are utilized. TRL (Through-Reflect-Line) calibration standards are designed and printed on both 0° and 90° oriented substrates to improve the accuracy by calibrating in the same transmission medium. Figure 2.7 shows the printed TRL standards and 20 mm long microstrip line. Table 2.3 shows the length of the standards and the frequency range of the delay lines corresponding to 45°-135° phase delays. Reference planes are shifted in order to exclude the effect of GCPW pads and GCPW-to-MS transition. WinCal XE software is used for multi-line TRL calibration.

Figure 2.8 shows the comparison of the simulated (black) and measured S_{21} per cm length for microstrip lines with different FDM directions. Measured and simulated microstrip

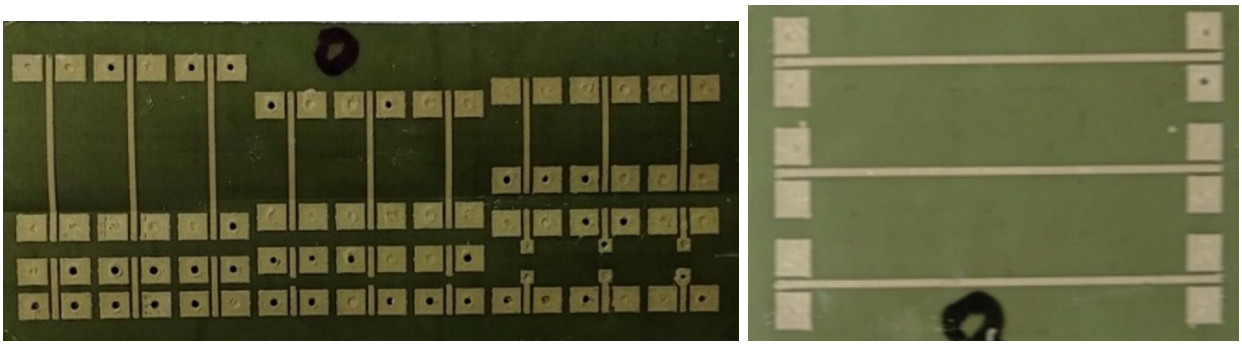

((a)) ((b))

Figure 2.7: Printed (a) TRL standards and (b) microstrip line

lines have larger than 20 dB return loss through the frequency range. At 18 GHz, printed microstrip line has 0.052 dB/mm attenuation in the parallel case and 0.072 dB/mm in the perpendicular case, whereas calculated attenuation of copper microstrip line for the same substrate is 0.024 dB/mm. Despite the difference in the attenuation, loss of the printed microstrip line at 18 GHz shows that DDM feed networks are feasible for high-frequency applications such as Ku-band. Microstrip line model has been simulated for various conductivity values until good agreement between the simulation and measurement is achieved. Because of the good correlation between the simulation and measurement, effective conductivity is extracted as $1.75 \times 10^6 S/m.$ for parallel case, and $0.7 \times 10^6 S/m.$ for the perpendicular case. This corresponds to 60% decrease in the effective conductivity for the perpendicular case. In conclusion, ABS should be deposited along the direction of the conductive traces to achieve the highest effective conductivity. Figure 2.9 shows the percentage increase in the insertion loss vs. frequency as a result of FDM direction. There is 8% increase in the attenuation at 18 GHz for 90° orientation due to the increased edge roughness. Attenuation increases almost linearly as frequency increases. This shows that effect of surface and edge roughness caused by FDM direction will be even more pronounced at K-band and beyond.

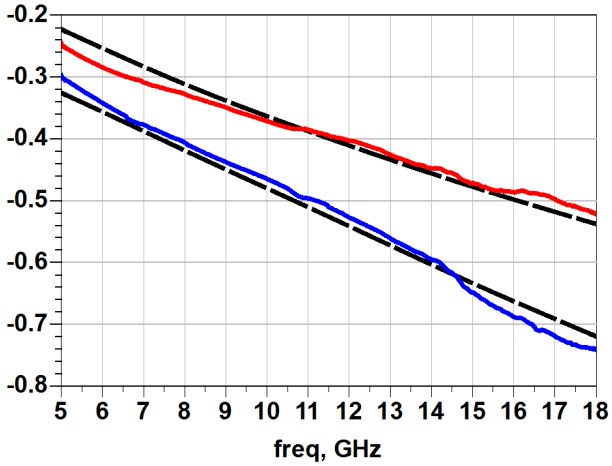

Figure 2.8: S_{21} (dB/cm) of 0° (red) and 90° (blue) FDM

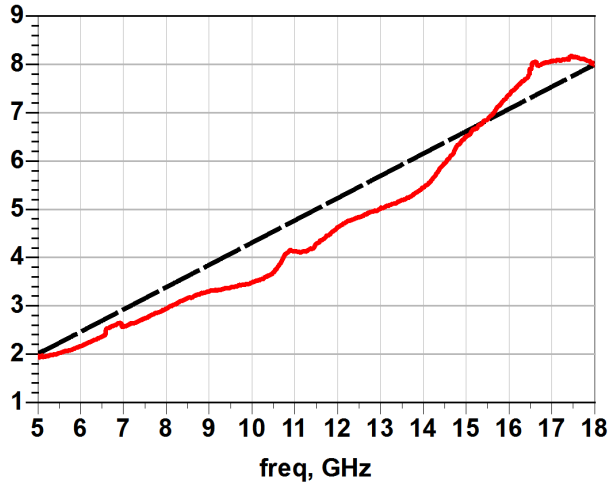

Figure 2.9: Percentage increase in insertion loss due to FDM direction

2.3 Concluding Remarks

Microstrip line characterizations show that printing ABS in parallel with the microstrip line direction minimizes the feed network loss. Printing ABS in perpendicular direction results in 8% increase in loss at 18 GHz, and 60% decrease in the effective conductivity. At 18 GHz, the printed microstrip line has 0.052 dB/mm attenuation which is comparable with the 0.024 dB/mm attenuation of copper microstrip lines over similar dielectric thicknesses. This performance implies $\approx 1.75 \times 10^6 S/m.$ conductivity within the Ku-band.

CHAPTER 3:

DIRECT DIGITAL MANUFACTURING OF MULTI-LAYER WIDEBAND KU-BAND SINGLE LAYER PATCH ANTENNAS

For satellite applications, Ku-band phased array antennas are widely utilized due to their advantages such as their high gain, beam-steering capabilities, and low interference. However, increasing cost and design complexity is challenges of the phased arrays. For example, packaging is difficult, and material properties such as thickness are fixed. In this chapter, design flexibilities and multi-layer printing capabilities of DDM are harnessed to address these problems. DDM multi-layer aperture-coupled single layer patch antenna is presented.

3.1 Antenna Design

In this chapter, an aperture coupled patch antenna is demonstrated with 30% bandwidth, 90% radiation efficiency and 6.5 dBi measured gain with center frequency at 15 GHz[1]. The wideband performance is achieved by employing a multi-layer printing approach that utilizes lower infill density (50%) ABS as the antenna substrate, and 100% infill density ABS for implementing the 50Ω microstrip lines with practical line widths. Reference [43] provides brief explanations to effects of each parameter.

[1]The content of this chapter is published in [40]. © 2017 IEEE. Reprinted, with permission, from M. Kacar, C. Perkowski, P. Deffenbaugh, J. Booth, G. Mumcu, and T. Weller, "Wide- band ku-band antennas using multi-layer direct digital manufacturing," in Proceedings of 2017 IEEE AP-S Symposium on Antennas and Propagation and USNC-URSI Radio Science Meeting, July 2017, pp. 1–2.

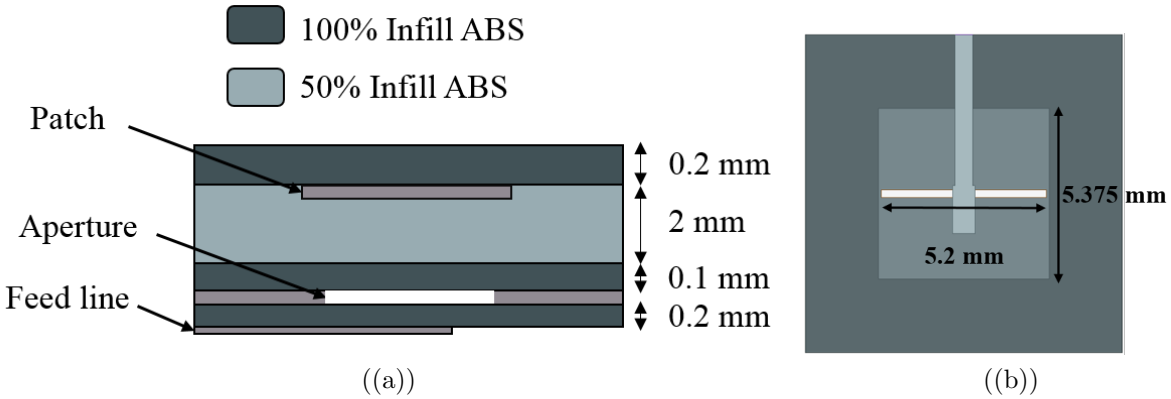

((a)) ((b))

Figure 3.1: (a) Substrate stack-up and (b) top view of the antenna

Figure 3.1 presents the substrate stack-up of the fully-printed 15 GHz aperture coupled patch antenna. It is important to note that the antenna is direct digital manufactured from top to bottom by utilizing the top layer as the base in printer bed. This allowed the exposure of the feed microstrip line to air for edge connector.

200 µm 100% infill ABS ($\varepsilon_r = 2.4$, tan$\delta = 0.006$) layer is printed prior to the patch as a base layer. 5.375 mm square patch is printed on the base layer. Square patch is commonly used in dual or circular polarization cases. Although this antenna is single polarized, a square patch is utilized to compare it to the dual-polarized antenna in next chapter. Compared to rectangular patch, square patch can cause higher cross-polarization levels; however, low cross-polarization levels are achieved with the utilized feeding technique. [41] has demonstrated that lowering the infill percentage of ABS results in decrease in the permittivity and loss tangent. 50% infill ($\varepsilon_r = 1.6$, tan$\delta = 0.003$) 1.925 mm ABS layer is utilized as antenna substrate since lower dielectric constant and loss tangent provides wider bandwidth, and higher radiation efficiency by decreasing the dielectric losses and surface wave excitation. In conventional manufacturing methods, substrate is drilled or micro-machining techniques such as lateral etching [44] is used to lower the dielectric constant, whereas, with FDM, lower dielectric constant can be easily achieved by lowering the infill percentage. Reducing printing time and material consumption are the other advantages of low infill substrates. Increase

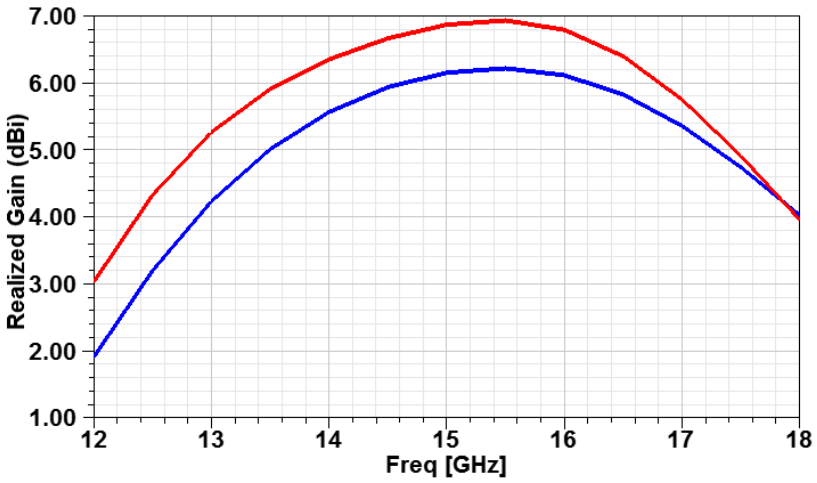

Figure 3.2: Gain for 50% (red) and 100% (blue) infill antenna substrates

in the directivity of the antenna should be also considered since lower dielectric constant substrate leads to larger patch size. In Figure 3.2, broadside realized gain is compared for 100% and 50% infill antenna substrates. For 100% infill simulations, patch size is adjusted to adjust the resonance frequency of the antenna. Antenna substrate thickness is kept the same in order to isolate the effect of the substrate thickness on radiation efficiency. In order to match the return loss, aperture width is increased to increase coupling between patch and slot. At the center frequency, realized gain of the antenna is improved by 0.7 dB by reducing the infill ratio. For a material with higher dielectric constant, the effect of lowering the infill ratio will be more pronounced.

Antenna substrate thickness has a strong effect on the impedance bandwidth. Thicker antenna substrates are utilized to achieve wider bandwidths. However, surface waves are excited as substrate thickness increases, as a result, radiation efficiency decreases and cross-polarization increases. Aperture coupling provides flexibility over the antenna substrate thickness since patch and feed line are on different substrates. FDM provides high flexibility over substrate thickness, while common fabrication techniques such as photolithography require utilization of laminates which are available only in few thickness options. By decreasing the layer thickness, flexibility over the substrate thickness can be increased. Figure

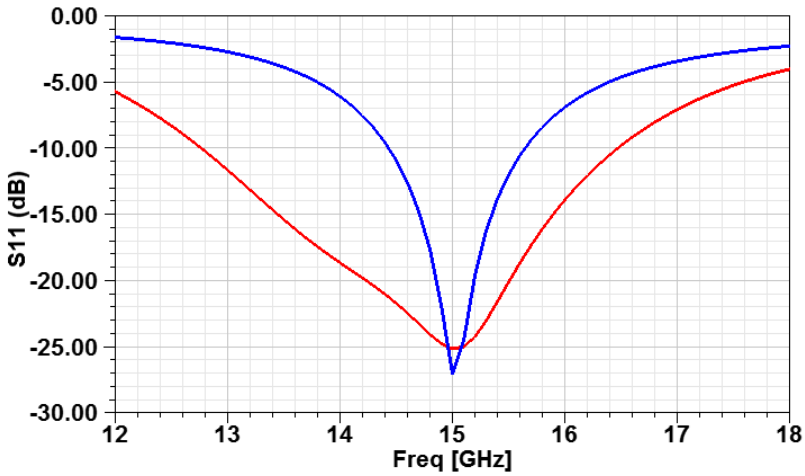

Figure 3.3: S_{11} for 2 mm (red) and 1 mm (blue) thick antenna substrates

3.3 demonstrates the effect of antenna substrate thickness on the bandwidth. Infill ratio (dielectric constant and loss tangent) of antenna substrate is kept the same for these simulations. There is 17.25% increase in the bandwidth as antenna thickness as substrate thickness increased to 2 mm from 1 mm. There is a slight (3.12%) decrease in the radiation efficiency for thicker substrates due to lower coupling of the aperture to the patch and surface wave excitation. Finally, over the antenna substrate, a thin (100 µm) 100% infill ABS layer is utilized prior to ground plane since the silver ink cannot be deposited on a porous surface due to its fluid characteristics.

In order to feed the antenna, aperture coupling technique is utilized due to its many advantages. Microstrip line and antenna are on different substrates and they are coupled through a slot in the common ground. This technique provides flexibility over antenna substrate (thickness and dielectric constant) and less spurious radiation from the feed line. Also, it sets a good example as a multi-layer direct digital manufactured RF device. Lumped element equivalent circuit model of aperture coupled patch antenna is shown in Figure 3.4. Aperture is represented as an R-L-C circuit since aperture is used as a resonator to enhance the impedance bandwidth. Aperture is followed by a series or parallel type R-L-C circuit representing the patch. An open-circuited stub is represented as a shunt capacitor used for

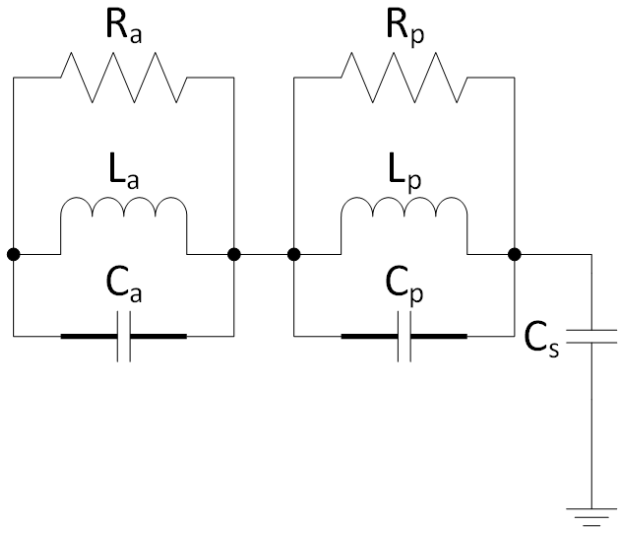

Figure 3.4: Equivalent circuit model of aperture coupled patch antenna

impedance matching. Wider feed line is utilized to increase the coupling. Stub length is tuned to move the locus to the center of the Smith Chart. A rectangular aperture is located in the center of the patch (maximum magnetic field) has a wide length (5.2 mm) to increase the coupling level between the feed line and antenna. Rectangular shape provides higher magnetic polarization. Figure 3.5 shows the input impedance of the antenna versus frequency for various aperture lengths in a Smith Chart plot. As the aperture size length, impedance locus passes over the center of the Smith Chart, and bandwidth increases. Compared to aperture length, width has a lower impact on the coupling. Although radiating aperture increases the bandwidth and coupling, it also increases the back-lobe radiation level. The designed antenna has 9.5 dB front-to-back ratio. Therefore, aperture size should be kept small after impedance matching is achieved. Also, front-to-back ratio can be improved by adding a reflector antenna or cavity over the feed line.

As feed line substrate, solid (100% infill) ABS substrate with 200 µm ($0.01\lambda_0$ at resonance frequency) utilized for less spurious radiation and low attenuation. Spurious radiation from feed line and especially from open-circuited stub is isolated from the patch by the ground plane. Since thin feed line substrates result in a narrower strip and higher atten-

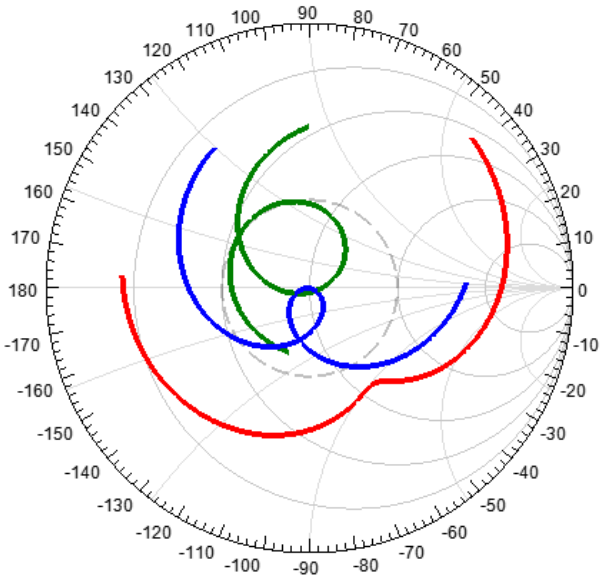

Figure 3.5: Z_{in} for 4 (red), 5 (blue) and 6 mm (green) long apertures

uation levels, substrate thickness should be decided considering the efficiency of the feed network.

In Figure 3.6, model of the antenna including the connector can be seen. The parallel printing direction was subsequently utilized in realizing the antenna feed to minimize the loss of the microstrip line which is additionally lengthened to accommodate the edge connector. Since the ground layer is not exposed, a section of feed line substrate near the edge is not printed to make the ground connection. Silver epoxy has been preferred in the microstrip-to-connector transition due to its low temperature curing properties.

The antenna is simulated with Ansys HFSS using modal solution type with network analysis. Solution frequency is selected as the highest frequency which is 18 GHz. Similar to the microstrip line simulations, maximum Delta-S is selected as 0.02. First order basis functions are used, and iterative solver is selected with 0.0001 relative residual. Antenna is simulated from 12 GHz to 18 GHz with interpolating sweep and discrete sweep for field calculations. For only antenna simulations, lumped port is used for excitation. Radiation boundary box has free-space quarter wavelength distance at the lowest simulation frequency

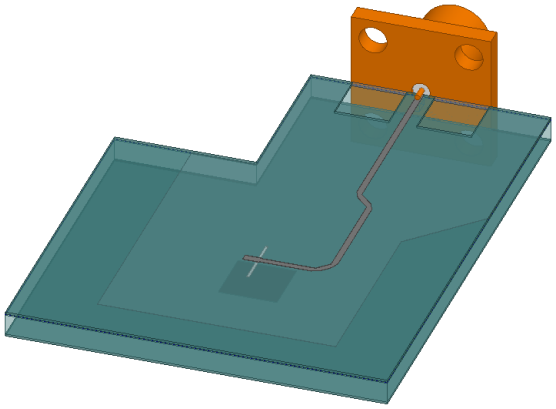

Figure 3.6: Single layer aperture coupled patch antenna model

(12 GHz) from all edges of the substrate. After the antenna is matched, the feed line is extended from the aperture to accommodate a connector. For more realistic simulations, the connector has been included in the model. A wave port at the end of the connector has been used for excitation in this model. Figure 3.7 shows the return loss and input impedance comparison of only antenna and antenna with the edge connector. Although there can be some reflections from microstrip-to-connector transition, 10 dB-RL bandwidth stays almost the same. In Figure 3.8, realized gain for co-polarization (solid) and cross-polarization (dashed) of only and full antenna model at the broadside direction can be seen. Due to the additional loss introduced by microstrip line and connector, full antenna model has around 0.7 dB lower gain than only the antenna. Cross-polarization level is higher for the full antenna model; however, cross-polarization isolation is still higher than 35 dB at the center frequency. There is 24% decrease in the efficiency due to the addition of microstrip line and conductor loss. Radiation patterns of only antenna and full antenna model at 15 GHz can be seen in Figure 3.9. Due to the larger ground plane, full antenna model has 16 dB front-to-back lobe radiation. It is significantly higher than only antenna model due to edge diffraction.

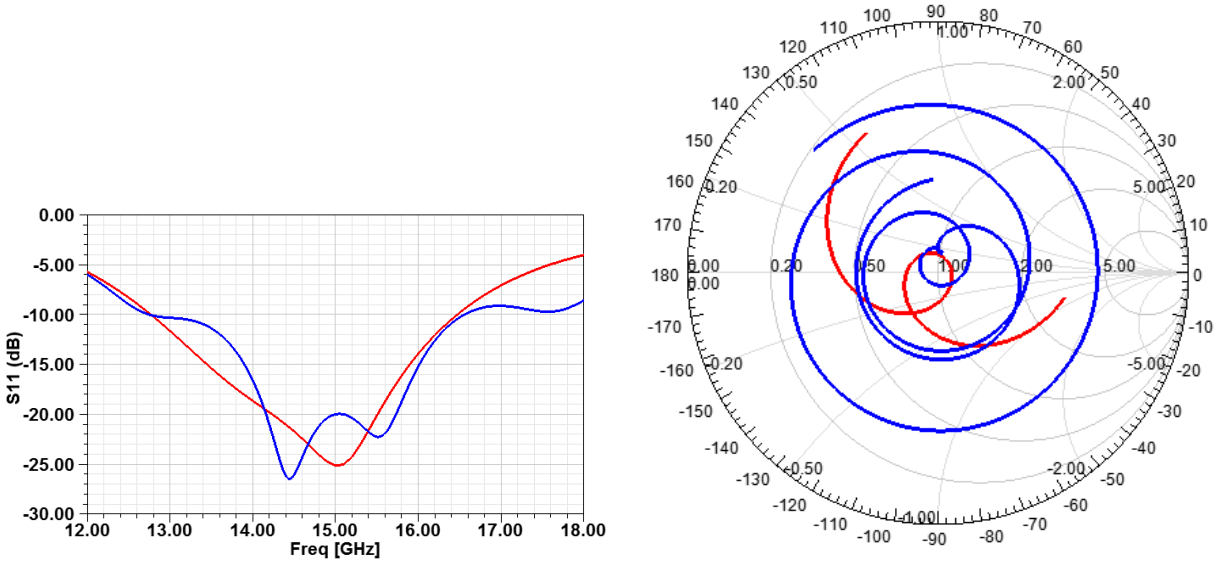

((a)) ((b))

Figure 3.7: S_{11} (dB) and Z_{in} of only (red) and full (blue) antenna model

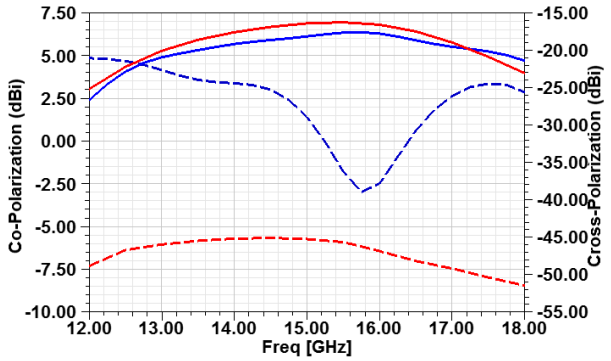

Figure 3.8: Co-pol and cross-pol gain of only (red) and full (blue) antenna

3.2 Tolerance Analysis

Compared to commonly used substrates from industry, printed substrate material has marginally higher tolerance due to voids and water inside the substrate. These defects can be minimized by fine adjusting of the printing settings; however, the effect of the deviation from the design values should be investigated in order to understand the possible discrepancies between the simulated and measured impedance bandwidth and radiation characteristics. Previous work shows that there can be ±3% change in the permittivity of 100% case. This

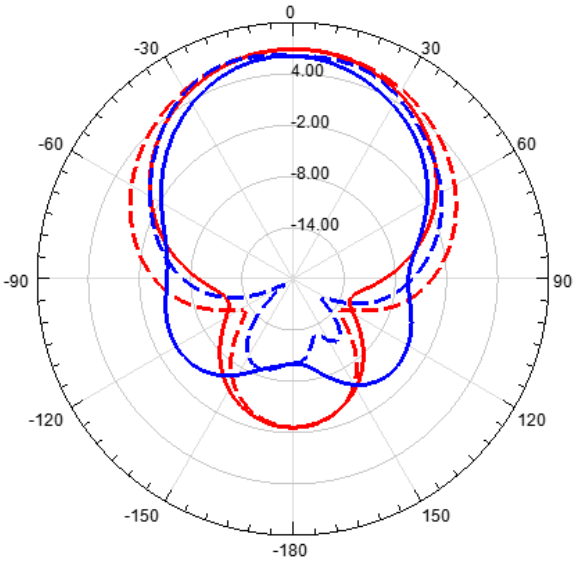

Figure 3.9: Radiation pattern of only (red) and full (blue) antenna model

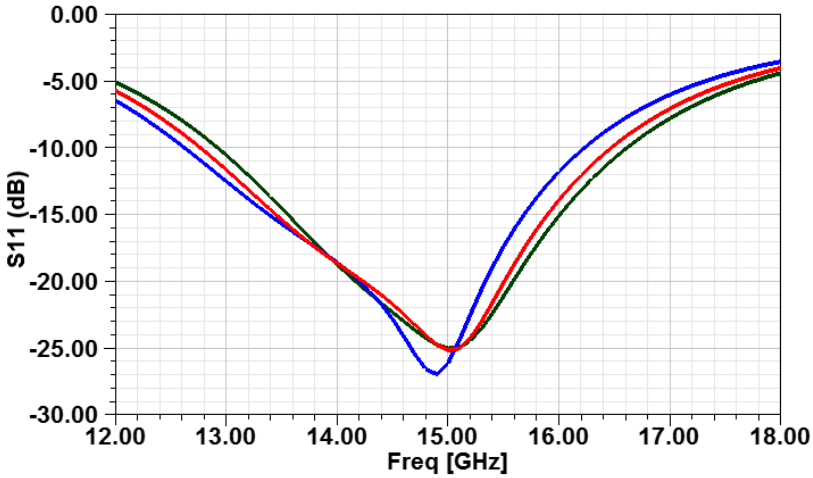

Figure 3.10: Effect of 3% increase (blue) and decrease (green) in ε_r on S_{11}

number is lower (±2%) for 50% infill substrate. In Figure 3.10, the effect of variation in dielectric constant on return loss of the antenna can be observed. 3% variation in dielectric constant causes around 0.67% shift at the resonant frequency. It shows that permittivity variation does not have a significant effect on the resonant frequency.

Other than tolerance of the material, manufacturing errors also cause discrepancy between the design and actual resonance frequency. One of them is the variation in the

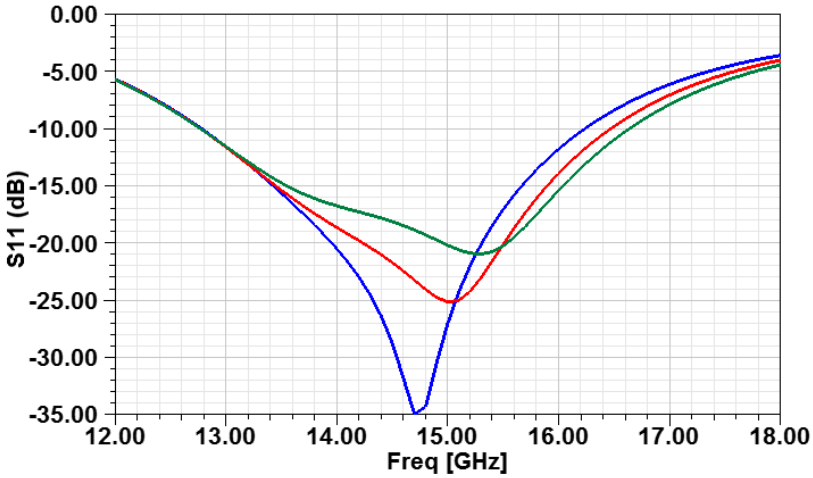

Figure 3.11: Effect of 5% deviation in antenna substrate thickness on S_{11}

substrate thickness. Change in the return loss of the antenna due to 5% increase (blue) and decrease (green) in the antenna substrate thickness can be observed in Figure 3.11. It results in 2% shift in the resonance frequency of the antenna. Although this error cannot be unregarded, thin layer thickness (25 µm) is utilized to minimize the substrate thickness variation.

Another source of discrepancy is the inaccuracy of the metallization dimensions such as patch, aperture size and microstrip line caused by micro-dispensing. Specifically, the effect of dimension variation will be more pronounced for higher frequency antennas. Valve opening and closing areas usually have blotching due to valve opening and closing speeds. Fine tuning of these parameters, blotching can be minimized. Also, a dimension can change significantly where the features like corners and bends are printed. Although printing with a low speed can provide better features, it is difficult to achieve sharp turns with this technique. Figure 3.12 shows the effect of 50 µm increase in the patch size (blue) , stub length (green) , and 25 µm increase in aperture length (orange). Most critical dimension is the patch size which changes the resonance frequency by 1.67%. Aperture size causes 1.33% shift in the resonance frequency.

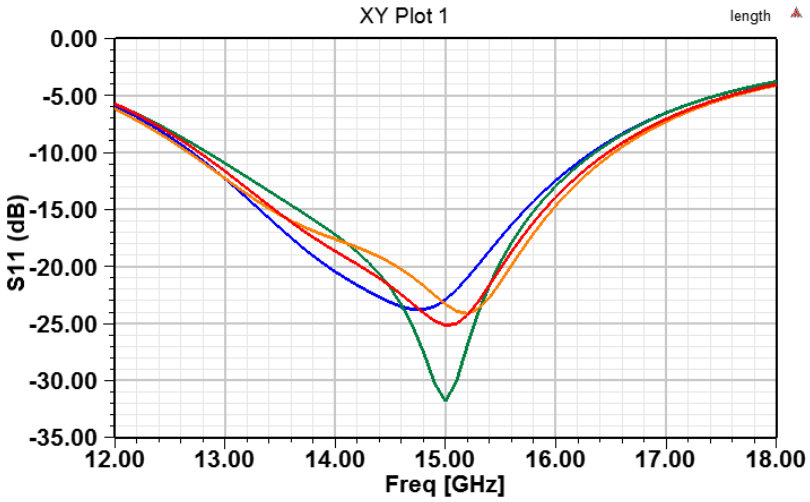

Figure 3.12: Effect of increase in patch, stub and aperture length on S_{11}

3.3 Power Handling Characterization

Power handling capability of the single patch antenna has been tested with 25 dBm input power at the resonant frequency (14.7 GHz). Figure 3.13 shows the thermal images of the top and bottom surfaces of the antenna recorded during steady-state. Maximum temperature is observed at the point where the microstrip line couples to the patch through the aperture which matches with the thermal simulation results. The maximum temperature is 28.1°C which is close to the room temperature (22°C). Whereas, glass transition temperature of the ABS is 105°C. Therefore, antenna can potentially operate at much higher input power levels. Due to the high radiation efficiency and low power dissipation in the conductor, high power handling capability is expected.

Figure 3.14 shows the simulated steady-state temperature distribution of the antenna. Using the simulation results from HFSS, Ansys Workbench software has been used in order to investigate the power handling capability of the antenna. The initial temperature is set to 22°C, and convection analysis is used. Heat transfer coefficient is adjusted as 10 W/(m^2·°C). Feed line face is selected as heat generation surface, and source frequency is selected. Other exposed faces are selected as heat flux surfaces. Maximum temperature has been observed at

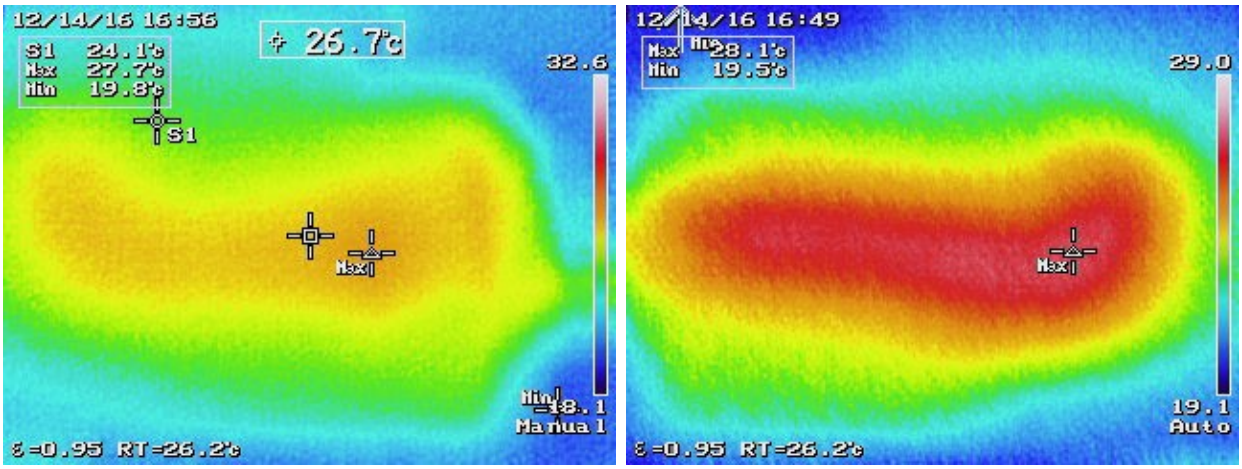

((a)) ((b))

Figure 3.13: Thermal image of (a) top and (b) bottom of the antenna

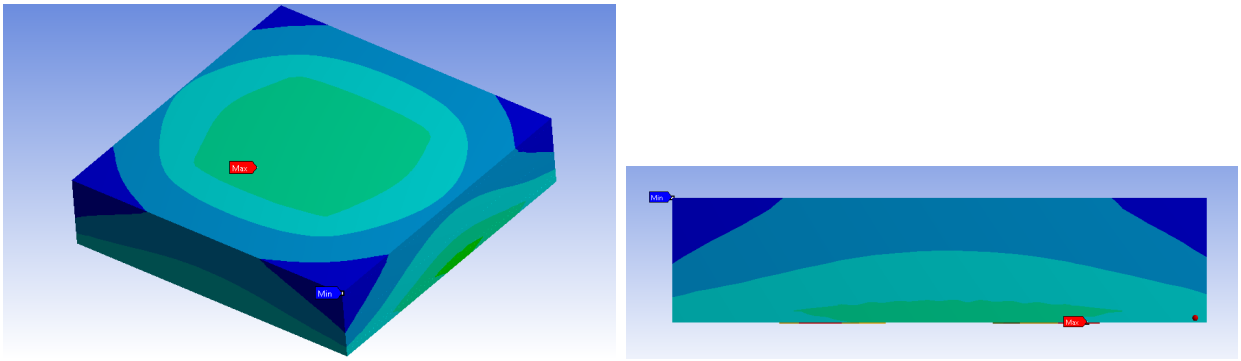

((a)) ((b))

Figure 3.14: Temperature distribution on (a) top and (b) side of the antenna

the point where feed line couples to the aperture. Initially, input power level is adjusted as 1 W from HFSS, and highest temperature has become 75°C. Input power level is increased to 1.5 W, where 98°C temperature has been observed which is very close to the glass transition temperature of ABS. Based on the simulations, the antenna can handle up to 1.5 W of input power.

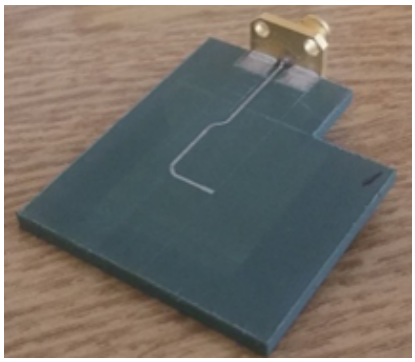

Figure 3.15: Fabricated antenna prototype

3.4 Experimental Verification

Figure 3.15 shows the printed antenna with the edge connector. Figure 3.16 presents the simulated and measured S_{11} performances. The antenna operates with 30% $|S_{11}|$ <-8 dB bandwidth (in comparison to the similar simulated $|S_{11}|$ <-10 dB bandwidth). The difference between the simulated and measured performance can be attributed to the slight geometrical variations in manufactured microstrip line stub length and width across the coupling slot. Nevertheless, a good bandwidth agreement is still achieved. Figure 2.3 shows the microscope image of the stub. Compared to the model, stub width is 10 µm smaller, and stub is 50 µm longer. Also, lower impedance line is shifted 125 µm towards the center of the antenna. Figure 2.3 shows the close view of the modified aperture according to microscope measurements. Figure 3.18 shows a better match with measured (blue) and simulated (red) return loss of the antenna by modifying the stub dimensions using the measurements.

Figure 3.19 depicts the measured and simulated H-plane radiation patterns with 6.5 dBi realized gain. Radiation efficiency is estimated as 90% due to the agreement between simulated and measured patterns and realized gain values. Figure 3.19 shows the measured and simulated broadside realized gain as a function of frequency and confirms the wideband performance.

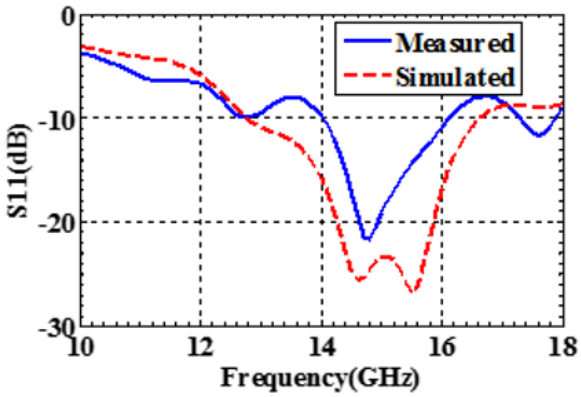

Figure 3.16: Measured and simulated S_{11} (dB)

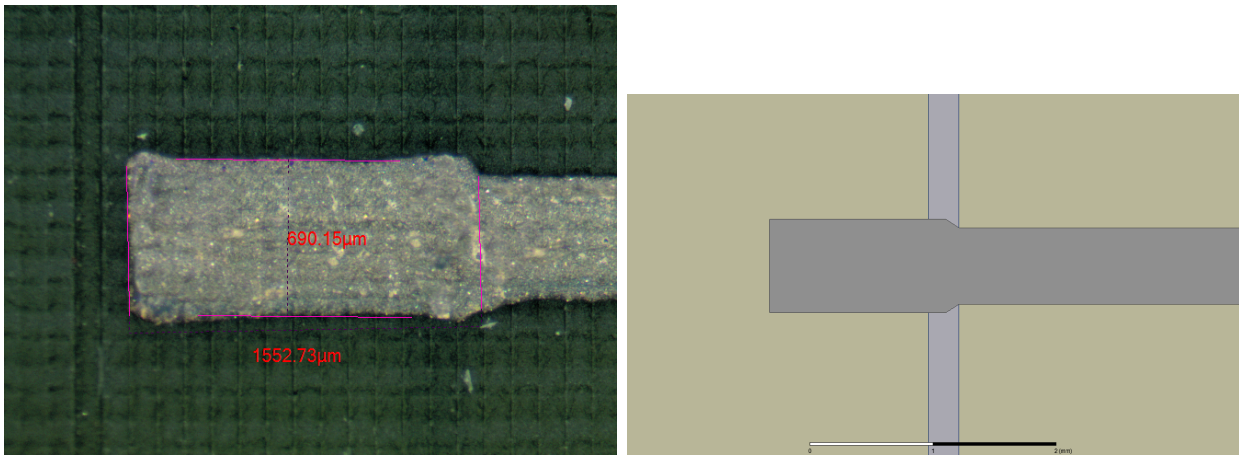

((a)) ((b))

Figure 3.17: (a) Microscope image of stub; (b) modified stub model

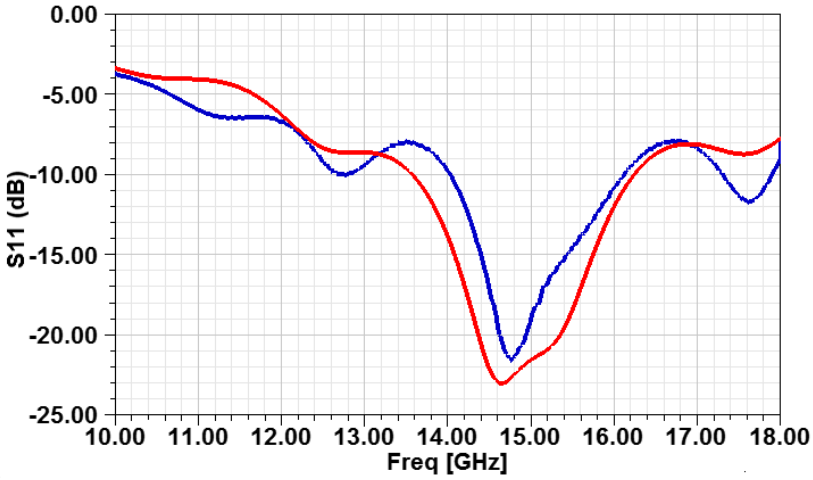

Figure 3.18: S_{11} of measured and simulated antenna with modified stub

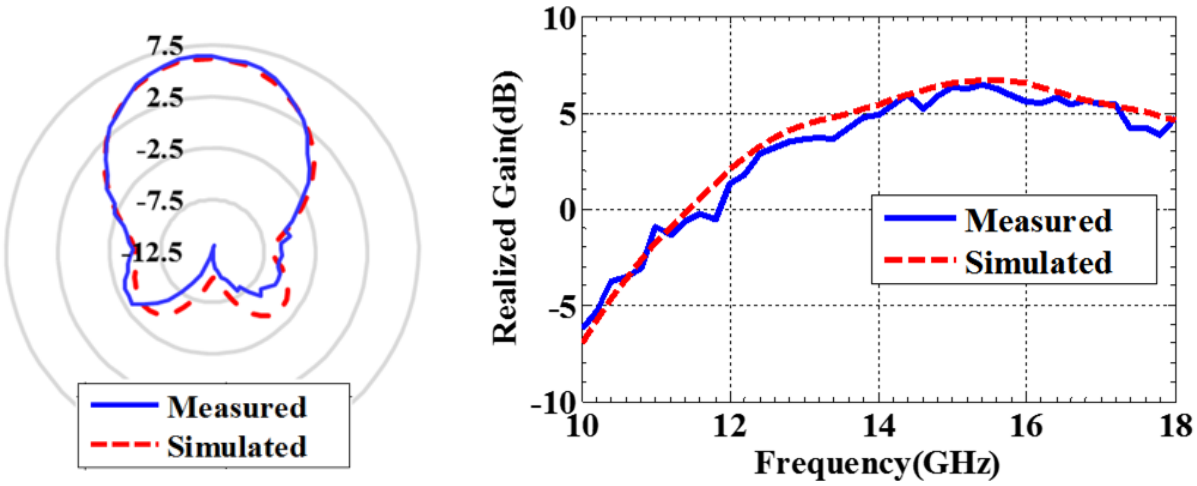

((a)) ((b))

Figure 3.19: (a) Realized gain pattern at 15 GHz; (b) Broadside realized gain

3.5 Concluding Remarks

Design and performance of a fully-printed Ku-band antenna manufactured by making use of a DDM approach that integrates fused deposition of ABS with micro-dispensing of CB028 are presented. Infill density variations and custom substrate thickness were utilized to achieve a wideband performance. 30% $|S_{11}|$ <-8 dB impedance bandwidth with 6.5 dBi realized gain and 90% estimated radiation efficiency at 15 GHz were achieved. Compared to existing work in literature, the presented antenna stands out as being fully-printed, operating within the Ku-band, and exhibiting high radiation efficiency with wide bandwidth performance.

CHAPTER 4:

DIRECT DIGITAL MANUFACTURING OF MULTILAYER WIDEBAND KU-BAND DUAL-LINEAR POLARIZED STACKED PATCH ANTENNA

The previous chapter demonstrated Ku-band single layer patch antenna with 30% bandwidth, 6.5 dBi realized gain and 90% radiation efficiency. Dual-polarization is commonly employed to increase the channel capacity. In order to achieve a similar bandwidth from a dual-linear polarized antenna, this chapter extends the design to a Ku-band stacked patch antenna. Dual-offset feed line design is employed to improve the isolation characteristics. The antenna is integrated with an SPDT switch to select polarization.

4.1 Antenna Design

Compared to the antenna demonstrated in Chapter 3, dual-linear polarization is utilized for this antenna design. In references [30, 45], dual-polarized aperture-coupled patch antennas with corner feeding and H-shaped apertures with 20-25% bandwidth have been demonstrated. Therefore, orthogonal feeding technique is utilized initially due to its simplicity; however, non-symmetric excitation causes high coupling between the feed lines and high cross-polarization levels. Figure 4.1 shows the orthogonally located feed lines. Surface wave excitation due to the thick antenna substrates also increases the coupling levels between the feed lines. Figure 4.2 shows broadside realized gain comparison of co-polarization (red) and cross-polarization (blue) levels. Beyond 16 GHz, there is a significant decline in the realized gain of the antenna. As explained in Chapter 3, antennas are designed and simulated using Ansys HFSS.

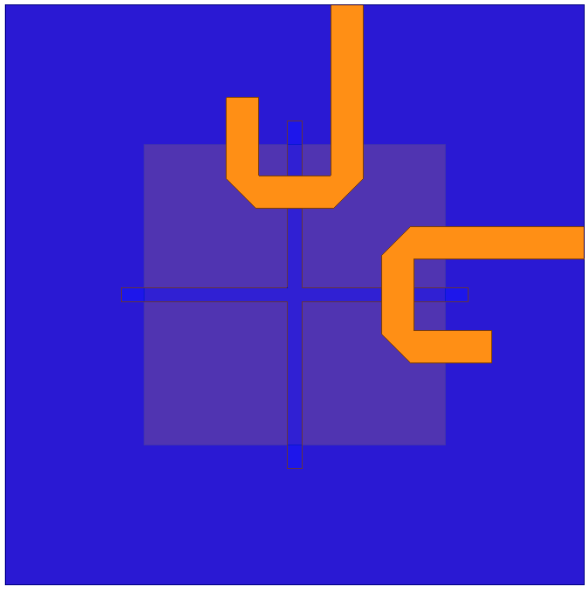

Figure 4.1: Aperture-coupled patch antenna with orthogonal feed lines

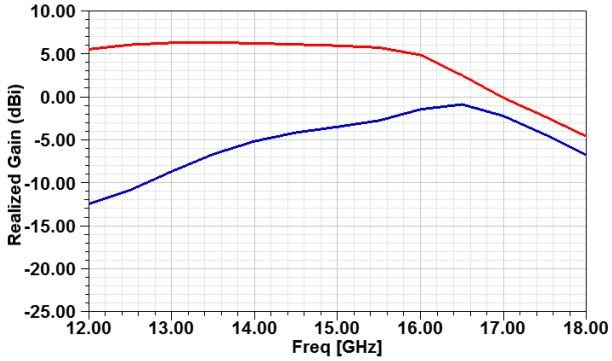

Figure 4.2: Co-pol and cross-pol gain for non-symmetric feed

Dual-offset feed lines do not suffer from high cross-polarization levels due to the symmetrical excitation. Open-circuited stubs are utilized to cancel the inductance from high coupling levels between aperture and patch. Figure 4.3 shows the dual-offset feed line design where 100 Ω lines exciting both sides of the patch. Feed lines are joined by a T-junction. To cross-over the feed lines where they intersect, a bridge made of ABS is printed. ABS bridge is optimized for minimum coupling and loss.

Figure 4.4 introduces the substrate stack-up of the dual-polarized stacked patch antenna. The antenna consists of 4 metallization layers which are upper and lower patches,

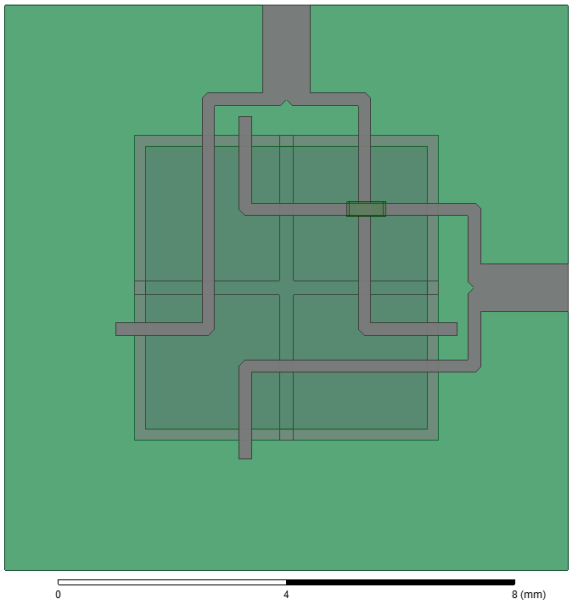

Figure 4.3: Aperture-coupled patch antenna with dual-offset feed lines

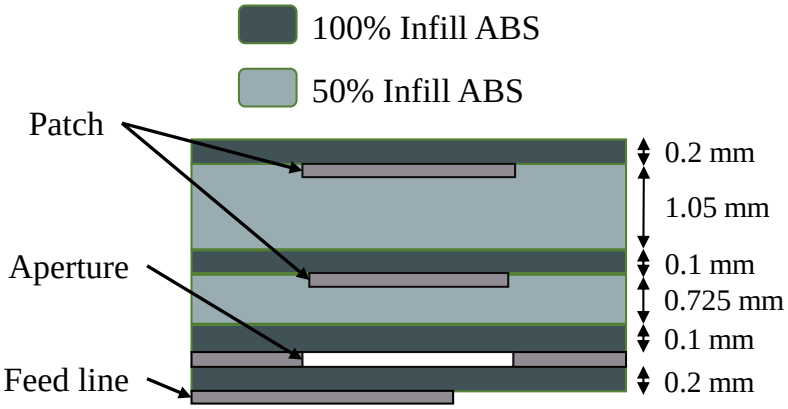

Figure 4.4: Substrate stack-up of the dual-polarized stacked patch antenna

ground layer and feed line. There are 6 layers of ABS which are antenna substrates, feed line substrate and base layers for metallization. Similar to the single layer patch antennas, a thin (200 µm) solid ABS layer is utilized as a base layer to the upper patch. Figure 4.5 shows the top view of the stacked patch antenna.

Dual-polarization decreases the bandwidth of the antenna with a thick substrate due to surface wave excitation and mutual coupling between the ports. Therefore, stacked

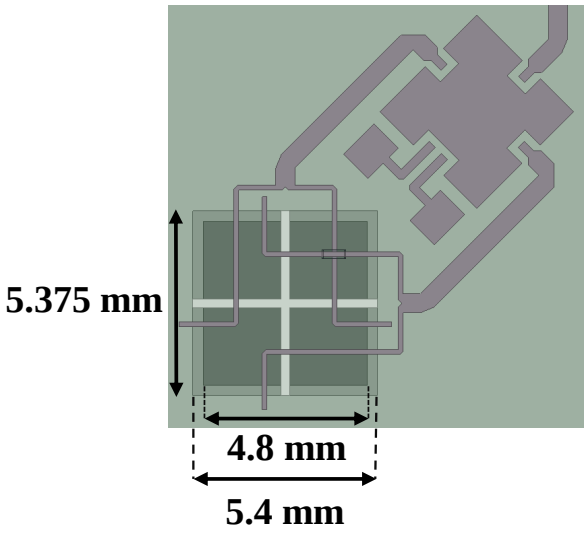

Figure 4.5: Top view of the dual-polarized stacked patch antenna

patch design is utilized to increase the bandwidth of the antenna. In reference [46], stacked patch antennas with wide apertures are investigated with a parametric study, and aperture-stacked patch antenna with 69% impedance bandwidth is demonstrated. In Chapter 3, it is shown that mutual resonance between the radiating aperture and patch creates an impedance locus at the Smith Chart. Stacked patch antennas with radiating apertures have another loop at the Smith Chart due to mutual coupling between the lower and upper patch antennas. Bringing these loops together in the Smith Chart and adjusting the coupling level provide a wide bandwidth performance. Figure 4.6 shows the input impedance of the stacked patch antenna. In this case, loops are inside each other with mutual resonance between the patches slightly dominating which resulted in the largest bandwidth. Figure 4.7 shows the comparison of single layer and stacked patch antenna designs for dual-polarization. Stacked patch provides 17% more impedance bandwidth than single layer patch antenna. For the stacked patch antenna design, design procedure in reference [46] has been followed. By changing the parameters such as patch sizes, antenna substrate thicknesses and aperture sizes, wide bandwidth performance is achieved.

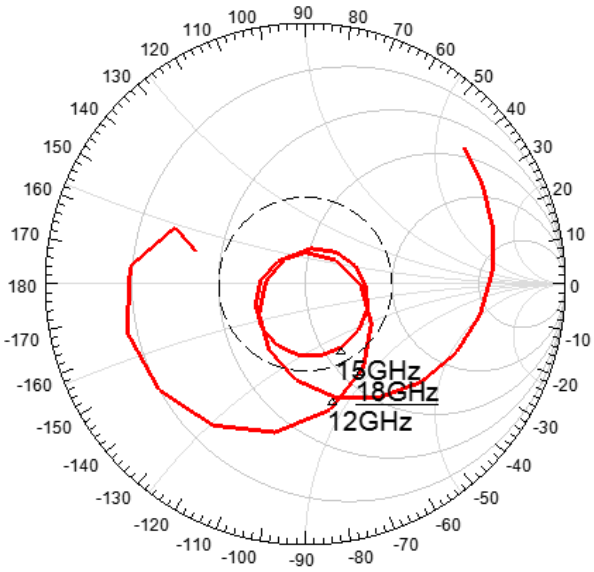

Figure 4.6: Z_{in} of the dual-polarized stacked patch antenna

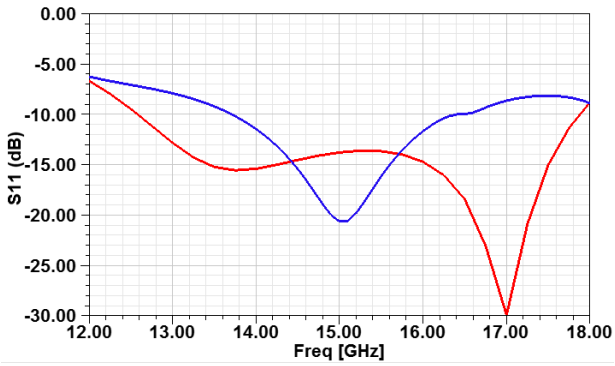

Figure 4.7: S_{11} of dual-pol single (blue) and stacked (red) patch antennas

Square patch shape is used in order to operate both polarizations in the same frequency range. The relative size of the patches determines the coupling levels which results in smaller or larger loops. Low coupling levels give small loop, while high coupling results in a big loop in the Smith Chart. A slightly larger upper patch antenna size (5.4 mm) compared to the lower patch antenna size (4.8 mm) provides a good coupling level. Varying the upper patch size significantly affects the higher-frequency loop, and changes the lower-frequency loop as well [46].

For antenna substrate thickness, thin substrates such as 75 µm to thick substrates such as 10 mm can be printed. Thickness should be chosen as an integer multiple of layer thickness (25 µm). As it is discussed in Chapter 3, thick antenna substrates increase the bandwidth. The infill ratio of the antenna substrates is adjusted to 50% since low dielectric constant and loss tangent decreases the dielectric losses, and increases the directivity of the antenna by increasing the patch size. 50% infill 1 mm thick dielectric substrate is printed in between the upper and lower patch antennas. Substrate thickness between the two patches affects the coupling level between the patches. Thicker substrates decrease the level of coupling, and higher-frequency loop becomes smaller [46]. Higher dielectric constant substrate increases the coupling level and causes larger loops.

Before printing the lower patch antenna, 100 µm thickness solid ABS layer is printed, since ink will leak into the porous substrate. Lower patch is a part of both mutual resonances, and varying this parameter affects both loops significantly. Therefore, lower patch size should be adjusted carefully. Size of the lower patch is slightly smaller than upper patch size and aperture length which provides lower coupling levels for wider bandwidth. 50% infill 0.75 mm thick ABS is printed on the lower square patch which is followed by a 100 µm thick solid ABS layer.

A ground plane with a resonating aperture used for bandwidth purposes. As the aperture length increases, the mutual coupling between the aperture and lower patch increases, the lower-frequency loop becomes larger, and loops get closer [46].

Thin (200 µm) microstrip feed line substrate is utilized for less spurious radiation; however, attenuation of the feed lines and minimum practical line thickness should be also considered. FDM direction is selected as 45° to the 100 Ω lines in order to keep the symmetry between the polarizations. The antenna is integrated with MACOM MASW-008322 DC-20 GHz SPDT switch in PQFN package (4 mm x 4 mm) to select the polarization. Figure 4.8 shows the return loss and insertion loss of the switch for two cases taken from the

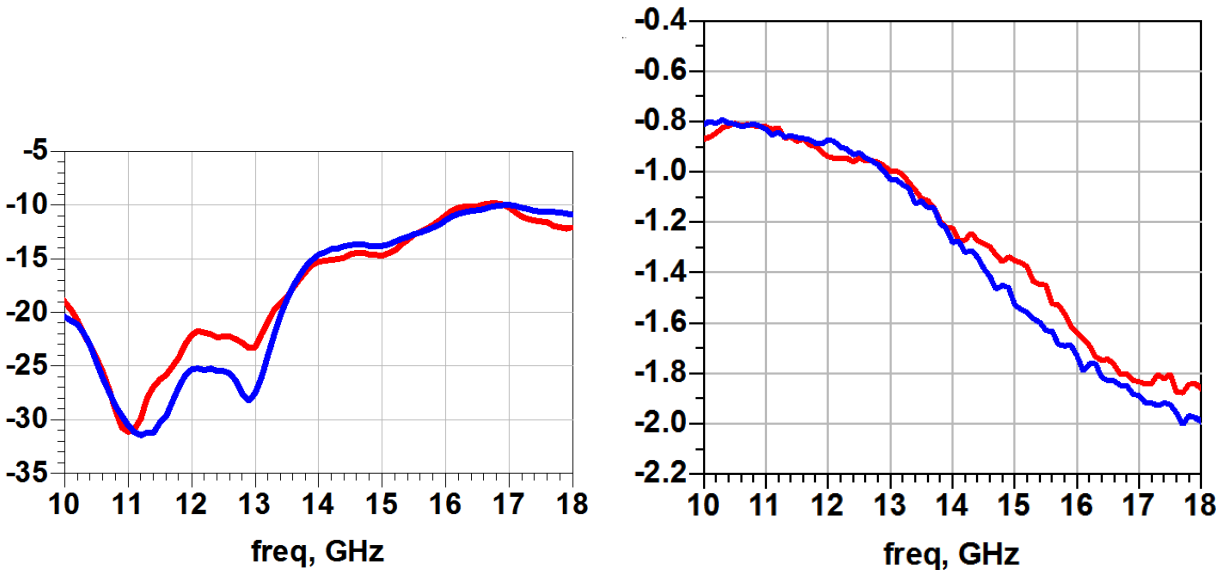

((a)) ((b))

Figure 4.8: (a) Return loss and (b) insertion loss of the SPDT switch

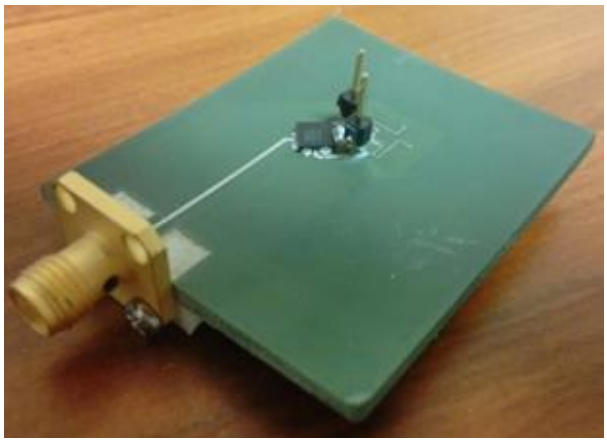

Figure 4.9: Printed dual-polarized aperture coupled stacked patch antenna

datasheet [47]. Gigalane Panel Mount SMA connector is utilized on the edge of the substrate for characterization. Figure 4.9 shows the printed and assembled dual-polarized aperture coupled patch antenna.

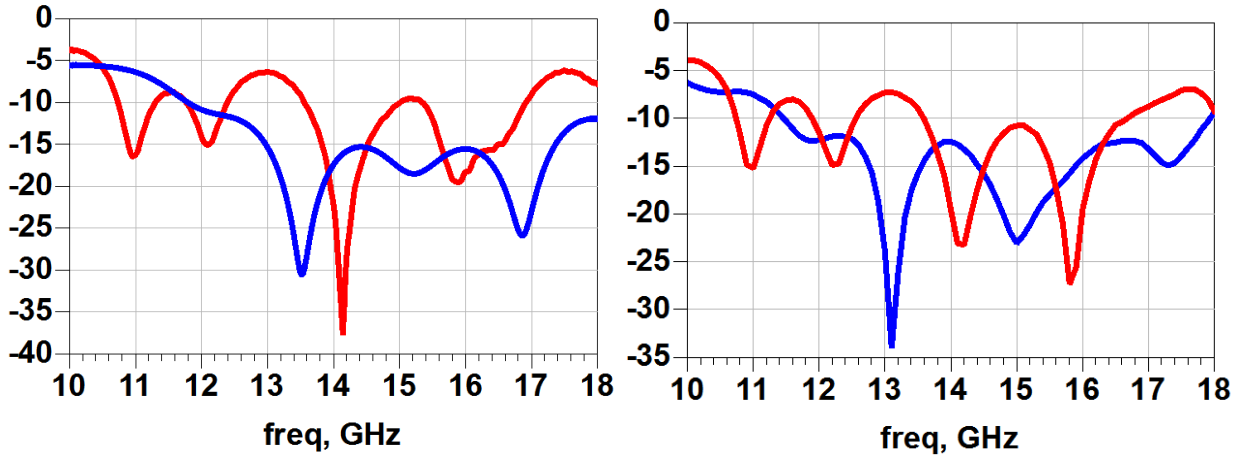

((a)) ((b))

Figure 4.10: S_{11} of measured (red) and simulated (blue) for both polarizations

4.2 Experimental Verification

Return loss of the antennas are measured from 10 to 18 GHz using Keysight E5063A Network Analyzer. Figure 4.10 shows the comparison of simulated and measured S_{11} (dB) for vertical and horizontal polarizations of the aperture coupled stacked patch antenna. Measured antenna has 24% bandwidth around 15.25 GHz, and return loss drops down to 6 dB at 13 GHz for both polarizations. Full antenna model without the switch is simulated in HFSS. The antenna has 35% $|S_{11}|$ <-10 dB bandwidth centered at 15.1 GHz. Figure 4.11 shows the comparison of S_{11} (dB) including the switch S-parameters supplied by the manufacturer. It provides a better match with the measured return loss; however, it doesn't explain the mismatch between the results. Non-ideal bridge fabrication is identified as the reason for discrepancy. It is more feasible to print a successful cross-over with wider microstrip lines. Substrate thickness can be increased to 300 µm without losing its performance.

Figure 4.12 presents the simulated and measured broadside realized gain versus frequency of the antenna for both polarizations and validates the wideband performance. Switch loss at Ku-band is subtracted from the simulated realized gain of the antenna. Due to the

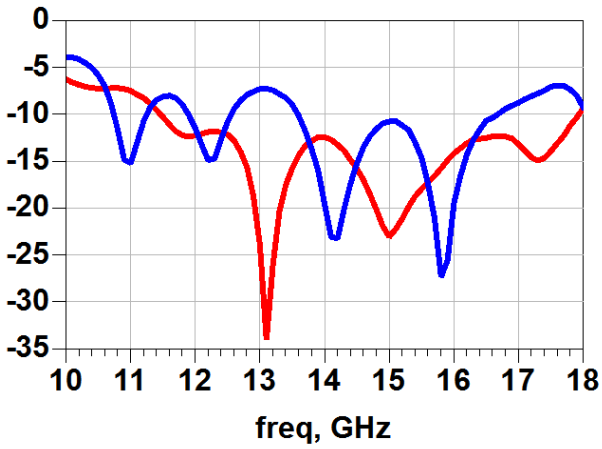

Figure 4.11: S_{11} of measurement (blue) and simulation with switch (red)

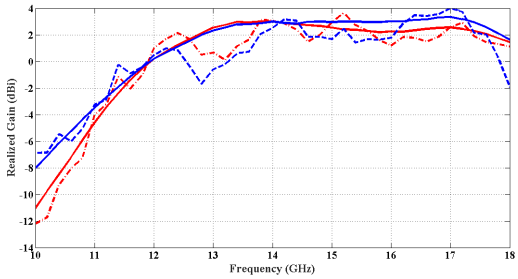

Figure 4.12: Simulated (solid) and measured (dashed) gain of antenna

good correlation in realized gain plots, realized gain of only the antenna can be extracted as 5.8 dBi at 15 GHz with 78% radiation efficiency.

4.3 Concluding Remarks

Fully-printed multi-layer wideband Ku-band dual-polarized aperture-coupled patch antenna is presented. The antenna is fabricated with FDM of ABS and micro-dispensing of CB028. Infill percentage of the ABS layers in antenna substrate is decreased to 50% in order to improve the bandwidth performance. Dual polarized patch antenna exhibits 5.8 dBi realized gain at 15 GHz and 78% radiation efficiency. This study shows that the fully-printed Ku-band antennas can exhibit high radiation efficiency, and antenna performance i.e. bandwidth can be improved using design flexibilities that additive manufacturing provides.

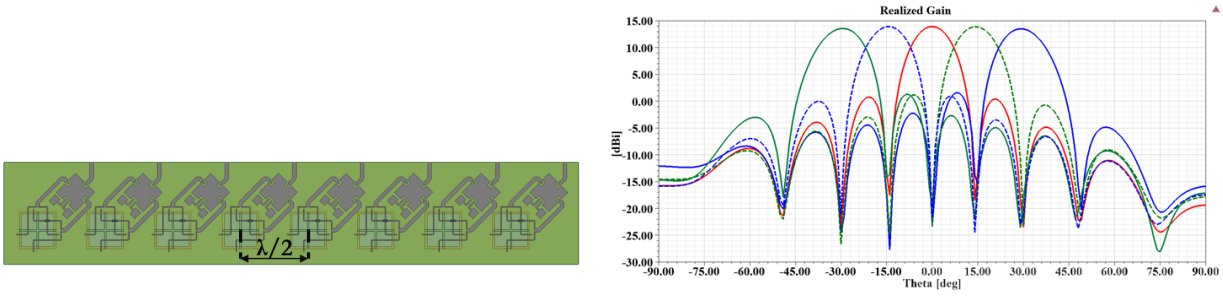

((a)) ((b))

Figure 4.13: (a) Bottom view and (b) realized gain of the 1x8 array

The antenna is suitable for 1-D array applications. Figure 4.13 shows the 1-D 8 element antenna array model and realized gain of the antenna obtained by full-wave simulations. The array has 14 dBi gain at broadside without including the switch loss, and beam can scan from -50 degrees to 50 degrees with up to 3 dB gain drop.

CHAPTER 5:

CONCLUSION

Fully-printed wideband Ku-band aperture-coupled patch antennas manufactured by integrating fused deposition modeling (FDM) of acrylonitrile butadiene styrene (ABS) thermoplastics with in-situ micro-dispensing of conductive silver paste (CB028) have been designed, and experimentally verified. Effective conductivity of the silver ink has been characterized through microstrip line characterizations. On 125 µm thick ABS substrate, attenuation of 0.052 dB/mm has been obtained at 18 GHz, which shows that high efficiency RF devices at Ku-band are feasible. Effect of ABS substrate deposition direction with respect to micro-dispensing direction has been demonstrated. Misalignment of FDM direction has degraded the effective conductivity up to 60% within the Ku-band and must be taken into consideration in antenna array feed network designs. Single and dual-polarized stacked patch antennas with bandwidth performance up to 35% and radiation efficiency up to 90% have been achieved by varying ABS infill ratios and resorting to multi-layer printing with custom substrate thicknesses. Dual-polarized antenna is integrated with an SPDT switch and utilized in an 8 element 1-D array simulation demonstrating high gain and beam-steering capabilities.

This work is distinguished from the recent work in the literature by being fully-printed, operating at higher microwave frequencies (i.e. Ku-band), and performing with high radiation efficiency and wide bandwidth. Design flexibilities provided by direct digital manufacturing such as multiple substrates with different infill ratios, in-situ printing of conductors, and custom substrate thicknesses have been harnessed which distinguishes this

work from the recently reported additively manufactured antennas. Utilizing this antenna in conformal surface, and 1-D or 2-D array applications with vertical stacking of T/R module components remain as a future study.

REFERENCES

[1] K. H. Church, N. B. Crane, P. I. Deffenbaugh, T. P. Ketterl, C. G. Neff, P. B. Nesbitt, J. T. Nussbaum, C. Perkowski, H. Tsang, J. Castro, J. Wang, and T. M. Weller, "Multimaterial and multilayer direct digital manufacturing of 3-D structural microwave electronics," *Proc. IEEE*, vol. 105, no. 4, pp. 688–701, April 2017.

[2] I. T. Ozbolat and Y. Yu, "Bioprinting toward organ fabrication: Challenges and future trends," *IEEE Trans. Biomed. Eng.*, vol. 60, no. 3, pp. 691–699, March 2013.

[3] E. Macdonald, R. Salas, D. Espalin, M. Perez, E. Aguilera, D. Muse, and R. B. Wicker, "3D printing for the rapid prototyping of structural electronics," *IEEE Access*, vol. 2, pp. 234–242, Dec 2014.

[4] T. Wohlers, *Wohlers report 2017 : 3D printing and additive manufacturing state of the industry : annual worldwide progress report.* Fort Collins, Colorado: Wohlers Associates, 2017.

[5] R. A. Street, T. N. Ng, D. E. Schwartz, G. L. Whiting, J. P. Lu, R. D. Bringans, and J. Veres, "From printed transistors to printed smart systems," *Proc. IEEE*, vol. 103, no. 4, pp. 607–618, April 2015.

[6] R. Sorrentino and O. A. Peverini, "Additive manufacturing: a key enabling technology for next-generation microwave and millimeter-wave systems [point of view]," *Proc. IEEE*, vol. 104, no. 7, pp. 1362–1366, July 2016.

[7] R. Sorrentino, P. Martin-Iglesias, O. A. Peverini, and T. M. Weller, "Additive Manufacturing of Radio-Frequency Components [Scanning the Issue]," *Proc. IEEE*, vol. 105, no. 4, pp. 589–592, Apr. 2017.

[8] P. I. Deffenbaugh, T. M. Weller, and K. H. Church, "Fabrication and Microwave Characterization of 3-D Printed Transmission Lines," *IEEE Microw. Wireless Compon. Lett.*, vol. 25, no. 12, pp. 823–825, Dec. 2015.

[9] F. Cai, Y. H. Chang, K. Wang, C. Zhang, B. Wang, and J. Papapolymerou, "Low-Loss 3-D Multilayer Transmission Lines and Interconnects Fabricated by Additive Manufacturing Technologies," *IEEE Trans. Microw. Theory Techn.*, vol. 64, no. 10, pp. 3208–3216, Oct. 2016.

[10] E. A. Rojas-Nastrucci, H. Tsang, P. I. Deffenbaugh, R. A. Ramirez, D. Hawatmeh, A. Ross, K. Church, and T. M. Weller, "Characterization and Modeling of K-Band Coplanar Waveguides Digitally Manufactured Using Pulsed Picosecond Laser Machining of Thick-Film Conductive Paste," *IEEE Trans. Microw. Theory Techn.*, vol. PP, no. 99, pp. 1–8, 2017.

[11] M. D'Auria, W. J. Otter, J. Hazell, B. T. W. Gillatt, C. Long-Collins, N. M. Ridler, and S. Lucyszyn, "3-D printed metal-pipe rectangular waveguides," *IEEE Transactions on Components, Packaging and Manufacturing Technology*, vol. 5, no. 9, pp. 1339–1349, Sept 2015.

[12] J. G. Hester, S. Kim, J. Bito, T. Le, J. Kimionis, D. Revier, C. Saintsing, W. Su, B. Tehrani, A. Traille, B. S. Cook, and M. M. Tentzeris, "Additively manufactured nanotechnology and origami-enabled flexible microwave electronics," *Proc. IEEE*, vol. 103, no. 4, pp. 583–606, April 2015.

[13] T. P. Ketterl, Y. Vega, N. C. Arnal, J. W. I. Stratton, E. A. Rojas-Nastrucci, M. F. Córdoba-Erazo, M. M. Abdin, C. W. Perkowski, P. I. Deffenbaugh, K. H. Church, and T. M. Weller, "A 2.45 GHz Phased Array Antenna Unit Cell Fabricated Using 3-D Multi-Layer Direct Digital Manufacturing," *IEEE Trans. Microw. Theory Techn.*, vol. 63, no. 12, pp. 4382–4394, Dec. 2015.

[14] J. Kimionis, M. Isakov, B. S. Koh, A. Georgiadis, and M. M. Tentzeris, "3D-printed origami packaging with inkjet-printed antennas for rf harvesting sensors," *IEEE Trans. Microw. Theory Techn.*, vol. 63, no. 12, pp. 4521–4532, Dec 2015.

[15] B. Sanz-Izquierdo and E. A. Parker, "3-D printing of elements in frequency selective arrays," *IEEE Trans. Antennas Propag.*, vol. 62, no. 12, pp. 6060–6066, Dec 2014.

[16] D. F. Hawatmeh, S. LeBlanc, P. I. Deffenbaugh, and T. Weller, "Embedded 6-GHz 3-D Printed Half-Wave Dipole Antenna," *IEEE Antennas Wireless Propag. Lett.*, vol. 16, pp. 145–148, 2017.

[17] P. Pa, Z. Larimore, P. Parsons, and M. Mirotznik, "Multi-material additive manufacturing of embedded low-profile antennas," *Electronics Letters*, vol. 51, no. 20, pp. 1561–1562, 2015.

[18] S. Moscato, R. Bahr, T. Le, M. Pasian, M. Bozzi, L. Perregrini, and M. M. Tentzeris, "Infill-Dependent 3-D-Printed Material Based on NinjaFlex Filament for Antenna Applications," *IEEE Antennas Wireless Propag. Lett.*, vol. 15, pp. 1506–1509, 2016.

[19] B. K. Tehrani, B. S. Cook, and M. M. Tentzeris, "Inkjet printing of multilayer millimeter-wave Yagi-Uda antennas on flexible substrates," *IEEE Antennas Wireless Propag. Lett.*, vol. 15, pp. 143–146, 2016.

[20] J. S. Silva, M. García-Vigueras, T. Debogović, J. R. Costa, C. A. Fernandes, and J. R. Mosig, "Stereolithography-Based Antennas for Satellite Communications in Ka-Band," *Proc. IEEE*, vol. 105, no. 4, pp. 655–667, Apr. 2017.

[21] D. M. Pozar, "Microstrip antenna aperture-coupled to a microstripline," *Electronics Letters*, vol. 21, no. 2, pp. 49–50, January 1985.

[22] D. Pozar and D. Schaubert, "Scan blindness in infinite phased arrays of printed dipoles," *IEEE Trans. Antennas Propag.*, vol. 32, no. 6, pp. 602–610, Jun 1984.

[23] D. Pozar, "A reciprocity method of analysis for printed slot and slot-coupled microstrip antennas," *IEEE Trans. Antennas Propag.*, vol. 34, no. 12, pp. 1439–1446, Dec 1986.

[24] P. Sullivan and D. Schaubert, "Analysis of an aperture coupled microstrip antenna," *IEEE Trans. Antennas Propag.*, vol. 34, no. 8, pp. 977–984, Aug 1986.

[25] R. Garg, *Microstrip antenna design handbook*. Boston, MA: Artech House, 2001.

[26] D. Pozar, *Microstrip antennas : the analysis and design of microstrip antennas and arrays*. New York: Institute of Electrical and Electronics Engineers, 1995.

[27] A. Adrian and D. H. Schaubert, "Dual aperture-coupled microstrip antenna for dual or circular polarisation," *Electronics Letters*, vol. 23, no. 23, pp. 1226–1228, November 1987.

[28] S. K. Padhi, N. C. Karmakar, C. L. Law, and S. Aditya, "A dual polarized aperture coupled circular patch antenna using a c-shaped coupling slot," *IEEE Trans. Antennas Propag.*, vol. 51, no. 12, pp. 3295–3298, Dec 2003.

[29] F. Croq and D. M. Pozar, "Millimeter-wave design of wide-band aperture-coupled stacked microstrip antennas," *IEEE Trans. Antennas Propag.*, vol. 39, no. 12, pp. 1770–1776, Dec 1991.

[30] S. Gao, L. W. Li, M. S. Leong, and T. S. Yeo, "A broad-band dual-polarized microstrip patch antenna with aperture coupling," *IEEE Trans. Antennas Propag.*, vol. 51, no. 4, pp. 898–900, April 2003.

[31] *ISO / ASTM52900-15, Standard Terminology for Additive Manufacturing - General Principles - Terminology*, Std., 2015. [Online]. Available: www.astm.org

[32] F. Calignano, D. Manfredi, E. P. Ambrosio, S. Biamino, M. Lombardi, E. Atzeni, A. Salmi, P. Minetola, L. Iuliano, and P. Fino, "Overview on additive manufacturing technologies," *Proc. IEEE*, vol. 105, no. 4, pp. 593–612, April 2017.

[33] J. C. S. Chieh, B. Dick, S. Loui, and J. D. Rockway, "Development of a Ku-band corrugated conical horn using 3-D print technology," *IEEE Antennas Wireless Propag. Lett.*, vol. 13, pp. 201–204, 2014.

[34] K. F. Brakora, J. Halloran, and K. Sarabandi, "Design of 3-D monolithic mmw antennas using ceramic stereolithography," *IEEE Trans. Antennas Propag.*, vol. 55, no. 3, pp. 790–797, March 2007.

[35] N. T. Nguyen, N. Delhote, M. Ettorre, D. Baillargeat, L. L. Coq, and R. Sauleau, "Design and characterization of 60-ghz integrated lens antennas fabricated through ceramic stereolithography," *IEEE Trans. Antennas Propag.*, vol. 58, no. 8, pp. 2757–2762, Aug 2010.

[36] E. A. Rojas-Nastrucci, J. T. Nussbaum, N. B. Crane, and T. M. Weller, "Ka-band characterization of binder jetting for 3-D printing of metallic rectangular waveguide circuits and antennas," *IEEE Trans. Microw. Theory Techn.*, vol. 65, no. 9, pp. 3099–3108, Sept 2017.

[37] B. Zhang, Z. Zhan, Y. Cao, H. Gulan, P. Linnér, J. Sun, T. Zwick, and H. Zirath, "Metallic 3-D printed antennas for millimeter- and submillimeter wave applications," *IEEE Transactions on Terahertz Science and Technology*, vol. 6, no. 4, pp. 592–600, July 2016.

[38] O. S. Kim, "Rapid prototyping of electrically small spherical wire antennas," *IEEE Trans. Antennas Propag.*, vol. 62, no. 7, pp. 3839–3842, July 2014.

[39] D. C. Lugo, R. A. Ramirez, J. Castro, J. Wang, and T. M. Weller, "3D printed multi-layer mm-wave dielectric rod antenna with enhanced gain," in *2017 IEEE International Symposium on Antennas and Propagation USNC/URSI National Radio Science Meeting*, July 2017, pp. 1247–1248.

[40] M. Kacar, C. Perkowski, P. Deffenbaugh, J. Booth, G. Mumcu, and T. Weller, "Wideband Ku-band antennas using multi-layer direct digital manufacturing," in *Proceedings of 2017 IEEE AP-S Symposium on Antennas and Propagation and USNC-URSI Radio Science Meeting*, July 2017, pp. 1–2.

[41] P. I. Deffenbaugh, "3D printed electromagnetic transmission and electronic structures fabricated on a single platform using advanced process integration techniques," Master's thesis, 2014.

[42] J. W. Stratton, "A study of direct digital manufactured RF/microwave packaging," Master's thesis, University of South Florida, 2015.

[43] P. David and M. Pozar, "A review of aperture coupled microstrip antennas: History, operation, development, and applications by," 1996.

[44] I. Papapolymerou, R. F. Drayton, and L. P. B. Katehi, "Micromachined patch antennas," *IEEE Trans. Antennas Propag.*, vol. 46, no. 2, pp. 275–283, Feb 1998.

[45] S. C. Gao, L. W. Li, P. Gardner, and P. S. Hall, "Wideband dual-polarised microstrip patch antenna," *Electronics Letters*, vol. 37, no. 20, pp. 1213–1214, Sep 2001.

[46] S. D. Targonski, R. B. Waterhouse, and D. M. Pozar, "Design of wide-band aperture-stacked patch microstrip antennas," *IEEE Trans. Antennas Propag.*, vol. 46, no. 9, pp. 1245–1251, Sep. 1998.

[47] *GaAs SPDT Switch*, MACOM, rev. V3. [Online]. Available: https://cdn.macom.com/datasheets/MASW-008322.pdf

APPENDIX A: LIST OF ACRONYMS

ABS	acrylonitrile butadiene styrene
AM	additive manufacturing
DDM	direct digital manufacturing
DMLS	direct metal laser sintering
FDM	fused deposition modeling
PGM	portable graymap format
SIW	substrate integrated waveguide
SLA	stereolithography
SLS	selective laser sintering

ABOUT THE AUTHOR

Merve Kaçar received the B.Sc. degree in Electrical and Electronics Engineering from Middle East Technical University (METU), Ankara, Turkey in 2015. She is currently working towards the M.Sc. degree in Electrical Engineering from University of South Florida, FL. Her research interests are additively manufactured antennas and RF systems.